

# Indium selenides for next-generation low-power computing devices

Seunguk Song<sup>1,2,3\*</sup>, Michael Altvater<sup>4,5</sup>, Wonchan Lee<sup>1,2</sup>, Hyeon Suk Shin<sup>2,6</sup>, Nicholas Glavin<sup>4,\*</sup>, and Deep Jariwala<sup>3,\*</sup>

<sup>1</sup>*Department of Energy Science, Sungkyunkwan University (SKKU), Suwon, 16419, Republic of Korea*

<sup>2</sup>*Center for 2D Quantum Heterostructures (2DQH), Institute for Basic Science (IBS), Sungkyunkwan University (SKKU), Suwon, 16419, Republic of Korea*

<sup>3</sup>*Department of Electrical and System Engineering, University of Pennsylvania, Philadelphia, Pennsylvania 19104, United States of America*

<sup>4</sup>*Air Force Research Laboratory, Materials and Manufacturing Directorate, Wright-Patterson Air Force Base, Ohio 45433, United States of America*

<sup>5</sup>*BlueHalo LLC, 4401 Dayton Xenia Rd. Dayton, Ohio 45432, United States of America*

<sup>6</sup>*Department of Chemistry, Sungkyunkwan University (SKKU), Suwon, 16419, Republic of Korea*

\*Correspondence should be addressed: [seunguk@skku.edu](mailto:seunguk@skku.edu) (S.S.), [nicholas.glavin.1@afrl.af.mil](mailto:nicholas.glavin.1@afrl.af.mil) (N.G.), and [dmj@seas.upenn.edu](mailto:dmj@seas.upenn.edu) (D. J.)

## Abstract

As silicon-based computing approaches fundamental physical limits in energy efficiency, speed, and density, the search for complementary materials to extend or replace CMOS technology has become increasingly urgent. While two-dimensional (2D) transition metal dichalcogenides have been extensively investigated, van der Waals indium selenides—particularly InSe and In<sub>2</sub>Se<sub>3</sub>—offer a compelling alternative with distinct advantages for next-generation electronics. Unlike conventional 2D semiconductors, indium selenides combine exceptional electron mobility (exceeding 1,000 cm<sup>2</sup>V<sup>-1</sup>s<sup>-1</sup>), high thermal velocity (>2×10<sup>7</sup> cm/s), thickness-tunable bandgaps (0.97-2.5 eV), and unique phase-dependent ferroelectric properties, enabling both high-performance logic and non-volatile memory functions within a single material system. This perspective critically evaluates the materials properties, fabrication challenges, and device applications of indium selenides, examining their potential to surpass silicon in ultra-scaled transistors through ballistic transport while simultaneously offering ferroelectric memory capabilities impossible in conventional semiconductors. We analyze recent breakthroughs in ballistic InSe transistors, tunnel field-effect transistors, and In<sub>2</sub>Se<sub>3</sub>-based ferroelectric devices for information storage, and identify key research priorities for addressing persistent challenges in scalable synthesis, phase control, and oxidation prevention. By bridging fundamental materials science with practical device engineering, we provide a roadmap for translating the exceptional properties of indium selenides into commercially viable, low-power computing technologies that can overcome the limitations of silicon while enabling novel computing architectures.

## Introduction

The miniaturization of silicon-based microelectronics faces concurrent challenges of limited device scalability and increasing energy consumption in advanced processing nodes, necessitating the exploration of novel materials solutions for future low-power computing hardware. The two-dimensional (2D) van der Waals indium selenides—InSe and In<sub>2</sub>Se<sub>3</sub>—have emerged as particularly promising candidates, offering advantages that potentially exceed those of both silicon and other widely studied 2D materials such as transition metal dichalcogenides (TMDs) of Mo and W<sup>1-5</sup>.

Indium selenides distinguish themselves through a unique combination of properties critical for next-generation electronics. First, their atomically thin nature allows for exceptional electrostatic gate control, mitigating short-channel effects that plague deeply scaled silicon transistors<sup>1,4,5</sup>. Second, InSe exhibits extraordinarily high electron mobility, with experimental values exceeding 1,000 cm<sup>2</sup>V<sup>-1</sup>s<sup>-1</sup> at room temperature<sup>6-8</sup>—superior to most TMDs and comparable to state-of-the-art silicon devices. This high mobility stems from InSe's remarkably low effective electron mass (~0.12m<sub>0</sub>), resulting in thermal velocities exceeding 2×10<sup>7</sup> cm/s that enable ballistic transport in nanoscale devices<sup>6,9-11</sup>. Third, the binary indium-selenium system offers a rich phase landscape with diverse structural configurations and electronic properties, allowing for precise engineering of device characteristics through phase and thickness control<sup>12-14</sup>.

Perhaps most significantly, certain phases of both In<sub>2</sub>Se<sub>3</sub> and InSe exhibit robust ferroelectric properties persisting down to the monolayer limit, combining semiconducting behavior with non-volatile memory functionality in a single material platform<sup>15-18</sup>. This integration of logic and memory capabilities within one material system offers an elegant path toward overcoming the energy-intensive data movement between separate logic and memory components in conventional von Neumann architectures<sup>16,19,20</sup>.

The materials diversity and functional richness of indium selenides have enabled recent advances in electronic devices specifically designed for logic and memory applications. For logic devices, significant progress has been demonstrated with InSe ballistic transistors achieving record-high transconductance values and current densities, making them promising candidates for sub-1 nm node integration<sup>6,10</sup>. Additionally, InSe-based tunnel field-effect transistors (TFETs) show potential for ultra-low power switching through sub-thermionic subthreshold characteristics<sup>21</sup>. On the memory front, In<sub>2</sub>Se<sub>3</sub> ferroelectric semiconductor field-

effect transistors (FeSFETs) leverage inherent ferroelectric properties for non-volatile data storage<sup>16,19</sup>, while ferroelectric tunneling junctions offer innovative approaches to resistance-based memory with high on/off ratios<sup>20</sup>.

In this perspective, we critically evaluate recent advances in indium selenide materials and devices, assessing their potential as cornerstones for beyond-silicon electronics focusing on low-power computing applications. We analyze the diverse phases and electronic structures of InSe and In<sub>2</sub>Se<sub>3</sub>, examine their thickness-dependent properties and ferroelectric characteristics, and address the ongoing challenges in materials synthesis and device integration. By bridging materials science fundamentals with device engineering considerations, this review aims to provide a comprehensive assessment of indium selenides' prospects for transforming future micro and nanoelectronics.

## Key Points

- Indium selenides uniquely combine exceptional electron mobility ( $>1,000 \text{ cm}^2\text{V}^{-1}\text{s}^{-1}$ ), high thermal velocity ( $>2 \times 10^7 \text{ cm/s}$ ), and diverse phase-dependent properties that make them superior to other 2D materials for ultra-scaled transistors and memory devices<sup>6,10</sup>.
- The polymorphic nature of InSe ( $\beta$ ,  $\gamma$ ,  $\varepsilon$  phases) and In<sub>2</sub>Se<sub>3</sub> ( $\alpha$ ,  $\beta$ ,  $\beta'$  phases) enables precise tuning of electronic and ferroelectric properties, offering unprecedented design flexibility for device engineers compared to conventional semiconductors with fixed properties<sup>12-14</sup>.
- Recent demonstrations of ballistic InSe transistors with 10 nm channels have achieved record-high transconductance (6 mS) and current densities that outperform other 2D materials and approach theoretical limits, validating indium selenides' potential for post-silicon logic devices<sup>6,10</sup>.
- The robust ferroelectricity in In<sub>2</sub>Se<sub>3</sub> (with Curie temperatures up to 700K) and emerging sliding ferroelectricity in InSe enable non-volatile memory functionality integrated with semiconducting properties—a combination unavailable in conventional materials that could fundamentally transform computing architectures<sup>16,19,20</sup>.
- Addressing the challenges of scalable synthesis, phase control, and oxidation prevention represents the critical path toward commercial implementation of indium selenide-based technologies for next-generation, low-power computing beyond the limitations of silicon CMOS.

## Properties of Indium Selenides across Diverse Phases

In this section, we provide an overview of materials structures and properties of indium selenides, highlighting their emergent and exciting properties while comparing with conventional bulk semiconductors and van der Waals semiconductors of 2D group-VI TMDs. Recently, layered 2D InSe and In<sub>2</sub>Se<sub>3</sub> have emerged as particularly interesting avenues for materials and device level exploration due to their superlative electronic and optical properties, relative thermodynamic stability at room temperature, and the ability to grow large crystals or thin films that are easily processable<sup>12-14</sup>. The larger indium selenide family of compounds exist in multiple different polymorphs and polytypes including layered (2D) InSe, In<sub>2</sub>Se<sub>3</sub>, In<sub>3</sub>Se<sub>4</sub> (Ref.<sup>22</sup>), and In<sub>4</sub>Se<sub>3</sub> (Ref.<sup>23</sup>). These 2D phases of indium selenides, in particular, are highlighted by different colors in the phase diagram given in **Fig. 1e**. Through this overview, we aim to provide insights into opportunities and limitations of indium-selenide-based materials and device technologies from an electronic materials perspective.

### *Polymorphism and electronic structures of InSe*

Indium (II) selenide (InSe) is a layered material wherein each layer is 4 atoms thick with a covalently bonded, honeycomb, in-plane lattice with D<sub>3h</sub> symmetry. Individual layers are van der Waals bonded in at least 3 distinct polytypes related by interlayer translations and 180° (modulo 120°) rotation operations shown in **Fig. 1a**. The different stacking orders and their space groups are given in **Table 1**. The electronic band structures for each InSe phase have been calculated density functional theory<sup>24-26</sup> and, in the cases of β-InSe and γ-InSe, corroborated with angle-resolved photoemission spectroscopy (ARPES) measurements<sup>27,28</sup>. As constituent layers share the same structure, the in-plane electronic properties of different stacking orders are similar with subtle differences arising from orbital overlap between layers. All of these phases have similar bandgaps, as β-InSe exhibits a direct band gap of 1.2 eV<sup>3</sup> about the Γ point, ε-InSe has an indirect gap of 1.4 eV<sup>29</sup> near the Γ point, and γ-InSe is a direct gap semiconductor with a gap around 1.3 eV<sup>30-33</sup> at the B-point in momentum space (shown in Table 1). Their low energy dispersions are similar to each other, exhibiting a steeper dispersion (lower effective mass) of the conduction band ( $m_e \sim 0.12$ ) compared to the valence band ( $m_h \sim 0.40$ ). It has been shown that transistors of 2D materials with ultra-scaled channels are intrinsically limited only by the scale length and thermal velocity of electrons in the

channel<sup>11,34,35</sup>. Thermal velocity of 2D electrons is dependent only on the temperature ( $T$ ) and effective electron mass ( $m_e$ ) as<sup>11,34,35</sup>:

$$v_{th} = \sqrt{\frac{\pi k_B T}{2m_e}}$$

Calculations of the effective masses of charge carriers in bulk InSe reveal very small effective electron mass of  $0.14 m_0$  and  $0.08 m_0$  for in-plane and out-of-plane conduction, respectively; much smaller than other 2D semiconductors such as MoS<sub>2</sub> and WSe<sub>2</sub> and comparable to 3D semiconductors like GaAs and Si. Although  $\gamma$ -InSe has received the most attention, all three of the InSe phases are expected to demonstrate high in-plane electron mobility due to their low effective masses and nearly identical low energy dispersions. Moreover, although the constituent layers of InSe are the same, the different symmetries of the polytypes give rise to different physical properties. For example, the lack of inversion symmetry in the  $\epsilon$  and  $\gamma$  phases allows for non-linear optical effects such as second harmonic generation<sup>36</sup> and piezophototronic effect<sup>37</sup> compared to  $\beta$ -InSe. Additionally, the non-centrosymmetry allows additional vibrational modes to be Raman active in the  $\gamma$  and  $\epsilon$  polytypes which can couple with other dipolar excitations. Unlike the group-VI TMDs previously mentioned, where reducing the thickness to monolayer opens a direct band gap, the monolayer bandgap of InSe is indirect at 2.4 eV<sup>29-33,36,38</sup>. Due to this, few and multilayer InSe tend to be the preferred material for electronic applications<sup>39</sup>, as discussed later.

**Table 1. Electronic properties of indium selenides<sup>29-33,36,38</sup>**

Material	Space Group	Ferroic	Bulk Band Gap (eV)	Monolayer Band Gap (eV)	Effective electron mass ( $m_0$ )	Thermal velocity (cm/s)
$\beta$ -InSe (2H)	P6 <sub>3</sub> /mmc	No	1.2 (direct)	2.4 (indirect)	0.12	$2.4 \times 10^7$
$\epsilon$ -InSe (2H)	P6 $\bar{m}$ 2	Yes	1.4 (indirect)	2.4 (indirect)	0.12	$2.4 \times 10^7$
$\gamma$ -InSe (3R)	R3m	Yes	1.3 (direct)	2.4 (indirect)	0.12	$2.4 \times 10^7$
$\alpha$ -In <sub>2</sub> Se <sub>3</sub> (2H or 3R)	P6 <sub>3</sub> /mc or R3m	Yes	1.3 (direct)	1.5 (direct)	0.13	$2.3 \times 10^7$
$\beta$ -In <sub>2</sub> Se <sub>3</sub> (1T or 2H or 3R)	P3 $\bar{m}$ 1 or P3 $\bar{m}$ 1 or R3 $\bar{m}$	No	1.4 (direct)	1.6 (direct)	0.12 (theory)	$2.4 \times 10^7$
$\beta'$ -In <sub>2</sub> Se <sub>3</sub> (2H or 3R)		Yes	0.97 (indirect)	2.5 (indirect)	0.21	$1.8 \times 10^7$

### ***Structural complexity and ferroelectricity of In<sub>2</sub>Se<sub>3</sub>***

Polymorphism in the In<sub>2</sub>Se<sub>3</sub> compound is more complicated than in the monoselenide as there are multiple possible structural configurations of each quintuple layer (Se-In-Se-In-Se) in addition to different stacking orders. Thus, the identification and refinement of structural parameters and resulting electronic properties of these polymorphs has been the focus of much research during the past century. The three most commonly reported phases of In<sub>2</sub>Se<sub>3</sub> are  $\alpha$ -In<sub>2</sub>Se<sub>3</sub>,  $\beta$ -In<sub>2</sub>Se<sub>3</sub>, and  $\gamma$ -In<sub>2</sub>Se<sub>3</sub>. In  $\alpha$ -In<sub>2</sub>Se<sub>3</sub>, one plane of In atoms are octahedrally coordinated and the other forms tetrahedra with the Se atoms (see **Fig. 1b**). In  $\beta$ -In<sub>2</sub>Se<sub>3</sub>, both planes of In atoms are octahedrally bonded to Se atoms. The  $\gamma$  phase of In<sub>2</sub>Se<sub>3</sub> exhibits a nonlayered (3D) crystal structure and remains stable when cooled to room temperature.

Additionally, the  $\alpha$  and  $\beta$  phases of In<sub>2</sub>Se<sub>3</sub> can exhibit different stacking orders.  $\alpha$ -In<sub>2</sub>Se<sub>3</sub> can form both 2H and 3R layered structures (P<sub>6</sub><sub>3</sub>/mc and R<sub>3</sub>m space groups, respectively) while  $\beta$ -In<sub>2</sub>Se<sub>3</sub> can adopt 1T, 2H, or 3R lattices (P $\bar{3}$ m1, P $\bar{3}$ m1, and R $\bar{3}$ m space groups, respectively)<sup>40</sup>. The different phases and their properties are listed in **Table 1**. In their monolayer form,  $\beta$ -In<sub>2</sub>Se<sub>3</sub> polytypes are centrosymmetric, whereas  $\alpha$ -In<sub>2</sub>Se<sub>3</sub> are non-centrosymmetric. This non-centrosymmetry gives rise to inherent electrical polarization even in a monolayer  $\alpha$ -In<sub>2</sub>Se<sub>3</sub><sup>15,41</sup>. The stability of the In<sub>2</sub>Se<sub>3</sub> phase depends strongly on the orientation, as  $\alpha$ -In<sub>2</sub>Se<sub>3</sub> is stable at room temperature until approximately 200°C, irreversibly transforming into the  $\beta$  phase above this temperature. Upon further heating, the 3D  $\gamma$ -In<sub>2</sub>Se<sub>3</sub> phase becomes the most stable above 650°C.

Ferroelectricity is a unique property of some materials, characterized by a spontaneous electrical polarization that can be reversed by the application of an external electric field. In  $\alpha$ -phase In<sub>2</sub>Se<sub>3</sub>, the third-layer Se atoms deviate from their centrosymmetric positions to achieve a more stable potential energy state. When an external electric field is applied, these Se atoms can shift either down-left or up-right, depending on the field direction. This atomic displacement induces out-of-plane (OOP) and in-plane (IP) electrical polarizations, corresponding to downward/upward and leftward/rightward orientations, respectively (**Fig. 1g**). In multilayer  $\alpha$ -In<sub>2</sub>Se<sub>3</sub>, the stacking configuration (i.e., 2H and 3R stacking) can further influence its ferroelectric properties<sup>42</sup>. The stacking order modulates interlayer interactions and charge redistributions, leading to variations in the motion of ferroelectric domain walls (FDWs)

in both IP and OOP directions. Notably, 3R-stacked  $\alpha$ -In<sub>2</sub>Se<sub>3</sub> exhibits IP movement of OOP FDWs, resulting in a broader electrical hysteresis (i.e., memory window) compared to its 2H-stacked counterpart. The curie temperature of  $\alpha$ -In<sub>2</sub>Se<sub>3</sub> is reported to  $\sim 700$  K<sup>43</sup>, which is higher than most of the 2D ferroelectric materials (e.g.,  $\sim 320$  K for van der Waals CuInP<sub>2</sub>S<sub>6</sub>), suggesting its robust operation at higher temperatures (see the comparisons of 2D ferroelectric materials in **Fig. 1f** and **Table S1**).

In the case of  $\beta$ -phase In<sub>2</sub>Se<sub>3</sub>, the bulk crystal is centrosymmetric; however, its surface can develop periodic nanostripes that break inversion symmetry, forming a metastable  $\beta'$  phase. This  $\beta'$  phase is similar to the  $\beta$  phase with a small displacement of the central Se atoms<sup>44,45</sup>. As this displacement breaks the centrosymmetry of the  $\beta$ -phase, the  $\beta'$  phase exhibits in-plane (anti)ferroelectricity, which persists down to the monolayer limit and stable to 200 °C in both bulk and thin exfoliated flakes<sup>46-48</sup>. Further, due to an unusual competition between ferroelectric and antiferroelectric ordering<sup>49</sup>, the  $\beta'$  phase often exhibits antiparallel adjacent ferroelectric domains, forming a striped superstructure<sup>44,47,50,51</sup>. Depending on the relative size and number of alternating domains, the macroscopic crystal can be observed to be antiferroelectric, ferroelectric, or can be poled to become fully ferroelectric<sup>51,52</sup>. ARPES measurements of the  $\beta'$  phase shows a band gap of 0.97 eV (indirect) in the bulk with an effective electron mass as small as  $m_e \sim 0.21 m_0$ <sup>53</sup>, while the band gap of monolayer  $\beta'$ -In<sub>2</sub>Se<sub>3</sub> has been found to be 2.5 eV by scanning tunneling microscope (STM) measurements<sup>54</sup>. This gives the  $\beta'$ -In<sub>2</sub>Se<sub>3</sub> phase a larger range of possible band gap values and thus, more tunability than the  $\beta$ -In<sub>2</sub>Se<sub>3</sub> phase.

Moreover, small energy differences and energy barriers between different stacking orders and polymorphs can easily lead to the formation of stacking faults and phase impurity<sup>42</sup>; especially following mechanical processing. In addition, these polymorphs are capable of undergoing phase transitions driven by temperature, defects, or synthesis parameters, enabling further engineering of the ferroelectric properties within the material system. For instance, heterophase junctions composed of  $\alpha$  and  $\beta'$  structures facilitate enhanced non-volatile memory performance through band engineering. Although careful correlation between phase composition and its impact on electronic properties has not yet been demonstrated, proper control and characterization of indium selenide polymorphs and polytypes is expected to be important for producing reliable and reproducible device performance. To this end, Raman spectroscopy has been the primary tool used for determining the different crystalline phases.

However, closely spaced Raman frequencies and phase mixtures can make accurate determination of crystalline phases difficult through Raman spectroscopy alone<sup>55</sup>, requiring further characterization using other methods.

### ***Structure-driven ferroelectricity in InSe***

Multilayer van der Waals InSe also exhibits ferroelectric polarization through a mechanism known as sliding ferroelectricity, where the stacking sequence of atomic layer dictates the electrical polarization<sup>17,56-58</sup>. Specific stacking arrangements induce charge transfer between layers, resulting in an OOP spontaneous polarization. When these atomic layers slide relative to each other, altering their stacking sequence, the associated charge transfer reverses, thereby flipping the spontaneous polarization. This sliding ferroelectricity in InSe can be enhanced or emerged through Y doping<sup>17,56</sup> and layer-number engineering<sup>57</sup>.

### ***Quantum confined effects depending on thickness (band gap)***

One of the advantages of using 2D materials in electronics design is the tunability of their electronic and optical properties with material thickness. As 2D materials are thinned to atomic length scales, quantum confinement causes large changes in the electronic band structure. For example, the optical band gaps of TMDs such as MoS<sub>2</sub> and WS<sub>2</sub> increase from their bulk values of ~1.5 and ~1.4 eV (indirect) to ~1.9 and ~2.1 eV (direct) in their monolayer limits, respectively<sup>59,60</sup>. Similarly, the thickness dependence of the band gaps of  $\gamma$ -InSe and  $\beta$ -InSe have been measured to be ~1.3 eV (direct) in the bulk and increases to ~2.4 eV (indirect) in the monolayer limit<sup>6,61,62</sup> while  $\alpha$ -In<sub>2</sub>Se<sub>3</sub> increases from ~1.3 eV (direct) in bulk<sup>63</sup> to ~1.5 eV (direct) in a monolayer<sup>64</sup>. and  $\beta$ -In<sub>2</sub>Se<sub>3</sub> goes from ~1.43 eV (direct) to greater than ~1.58 eV (direct) (~1.58 eV was measured for bilayer)<sup>65</sup>. Unlike the TMDs which experience an abrupt transition from monolayer to bulk, these phases of InSe and In<sub>2</sub>Se<sub>3</sub> gradually transition over thicknesses approximately 10 nm, allowing for a high degree of band structure optimization.

The origin of the direct-to-indirect gap crossover in the InSe phases has been observed experimentally and studied theoretically and it has been found that the quantum confinement effect causes different valence bands to shift in energy at different rates with decreasing thickness. As layer number decreases from bulk, the valence band peaked at the  $\Gamma$  (or B) point gets pushed to lower energies, eventually transitioning below the next highest energy valence



band between 6-20 layers<sup>26,62,66</sup>. The valence band at low thicknesses has a maximum along the  $\Gamma$ -K direction, forming a distorted “Mexican hat” potential. This transition changes the band gap from momentum direct at bulk-like thicknesses to momentum indirect at low thicknesses. It has been noted from high-level DFT modelling that in the case of  $\gamma$ -InSe, in addition to this quantum confinement effect, In-In and In-Se bond lengths at the crystal surfaces also exhibit a thickness-dependence<sup>26</sup>. Indeed, experiment has shown anomalous behavior of interlayer-coupled vibrational modes as a function of thickness in this material<sup>67</sup>. Due to the reduced dimensionality, many-body effects and long-range forces have a stronger effect on optical and electronic properties. For example, Coulomb interactions and electron-phonon coupling are enhanced in the monolayer limit of InSe, leading to a dramatic increase in excitonic binding energy<sup>26</sup> and dark exciton luminescence<sup>61</sup>.

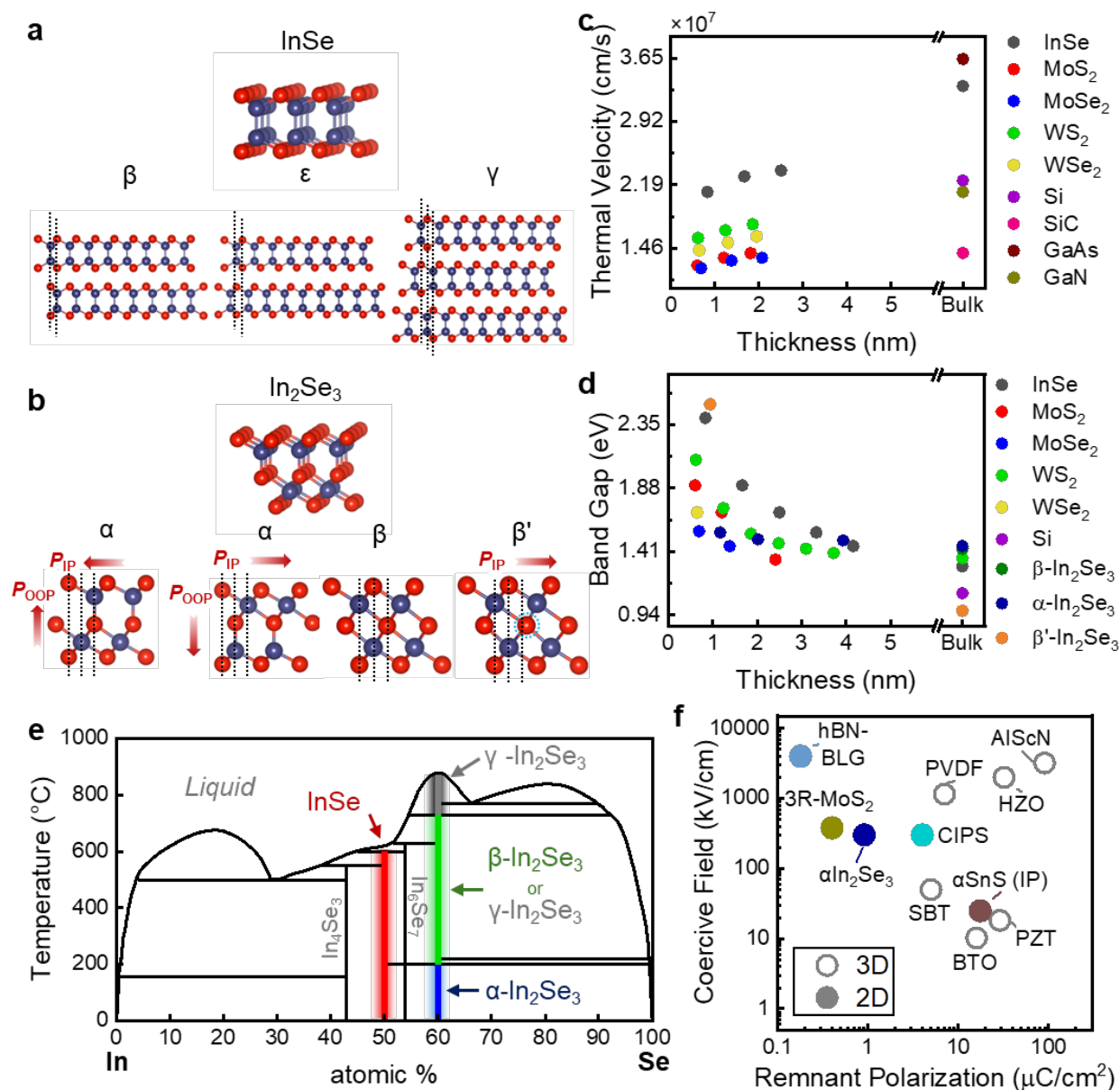
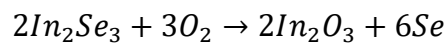
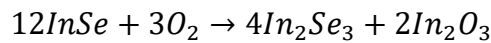


**Figure 1. Indium selenide structural phases and electronic properties.** (a) InSe monolayer structure (top) and different stacking orders ( $\beta$ ,  $\epsilon$ , and  $\gamma$ ) (bottom). Dashed lines highlight interlayer alignment of In and Se atoms. (b) 5-atom-thick layer of  $\text{In}_2\text{Se}_3$  (top) and three structural phases ( $\alpha$ ,  $\beta$ , and  $\beta'$ ). Two polarizations and associated lattice displacements of the  $\alpha$ -phase are given. Dashed lines highlight atomic positions within each layer of each different phase. (c) Thermal velocity as a function of thickness for InSe, semiconducting TMDs, and commonly used 3D semiconductors. (d) Thickness-dependent band gaps of the indium selenides compared with the semiconducting TMDs as well as bulk silicon. (e) Phase diagram for combinations of In and Se. The temperatures and compositions which form the 2D indium selenides of interest are highlighted in red, blue, and green for InSe,  $\alpha$ - $\text{In}_2\text{Se}_3$ , and  $\beta$ - $\text{In}_2\text{Se}_3$ , respectively. (f) Coercive field and remnant polarization of  $\alpha$ - $\text{In}_2\text{Se}_3$  compared with other 2D van der Waals ferroelectrics<sup>68-74</sup> (filled) and conventional 3D ferroelectrics<sup>75-78</sup> (opened). Here, all materials exhibit out-of-plane ferroelectricity, except for  $\alpha$ -phase SnS, which has in-plane ferroelectricity (labeled as "IP").

## Scalable Thin-Film Deposition

Although InSe and In<sub>2</sub>Se<sub>3</sub> exhibit attractive material properties, numerous challenges arise in their preparation. In particular, the inherent complexity of the In-Se phase diagram complicates the chemical synthesis of materials with the desired stoichiometry, as illustrated in **Fig. 1e**. Unlike 2D group-VI TMDs (e.g., MoS<sub>2</sub>) or 3D III-V compound semiconductors (e.g., GaN, GaAs, and InP), which exhibit only one stable polymorph, the binary In-Se system includes at least four stable phases (InSe, In<sub>2</sub>Se<sub>3</sub>, In<sub>6</sub>Se<sub>7</sub>, and In<sub>4</sub>Se<sub>3</sub>) at room temperature. This complexity hinders precise stoichiometric control during chemical synthesis, compromising the phase purity of the resulting crystal. Moreover, the instability of InSe under ambient conditions, particularly in the presence of water molecules and oxygen, presents a significant challenge due to its high susceptibility to oxidation. InSe and In<sub>2</sub>Se<sub>3</sub> spontaneously oxidize rapidly when exposed to air or moisture, following simple reactions:<sup>79</sup>



This oxidation process results in the formation of amorphous In<sub>2</sub>Se<sub>3</sub> or elemental Se, while converting the crystalline InSe or In<sub>2</sub>Se<sub>3</sub> into stable In<sub>2</sub>O<sub>3</sub>. Consequently, it is essential to have a thorough understanding of methods for preparing InSe or In<sub>2</sub>Se<sub>3</sub> with the desired stoichiometry and chemical purity. Furthermore, considering the scalability required for electronic device applications, achieving large-area synthesis of these materials with controlled thickness is equally important. From this perspective, this session aims to review chemical/mechanical exfoliation techniques, large-area thin film growth methods, and oxygen protective strategies for ensuring the realization of high-quality crystals.

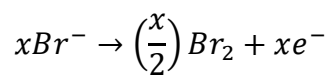
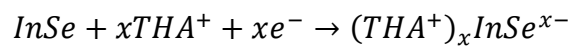
### *Mechanical/chemical exfoliations.*

Recent advancements in preparing 2D InSe and In<sub>2</sub>Se<sub>3</sub> nanosheets have explored various top-down techniques, including mechanical and chemical exfoliations from bulk single crystals. Regarding mechanical exfoliation, it often uses adhesive tapes to produce high-quality, single-crystalline few layers from mother crystal, suitable for fundamental studies. For example, thickness-dependent quantum confinement that affecting the band structure<sup>80</sup> and excitonic lasing properties<sup>81</sup> has been investigated in mechanically exfoliated InSe crystals. However, mechanical exfoliation typically yields small flakes (< 1,000 μm<sup>2</sup>) with limited scalability for

commercialization.

On the other hand, “liquid-phase exfoliation” uses solvents and ultrasonic energy to disperse layered materials into nanosheets. This approach can produce larger quantities of exfoliated material, making it more suitable for applications requiring bulk production. However, it may introduce defects or impurities, potentially affecting the material's intrinsic properties. A liquid-phase exfoliation using KOH, achieving thicknesses down to 7 nm for InSe is reported in 2018<sup>82</sup>. Liquid exfoliation in this study enables the production of few-layered InSe nanosheets with direct band gaps and large lateral sizes, which are essential for fabricating high-performance photoelectrochemical photodetectors. To prevent crystal's oxidation, one report presents that exfoliating InSe using a surfactant-free, deoxygenated low boiling point ethanol-water cosolvent system<sup>83</sup>. The preparation of high-quality InSe flakes facilitates exceptional photoresponsivity ( $\approx 5 \times 10^7 \text{ A W}^{-1}$ ) in photodetectors.

Another solution-processable method of “molecular intercalation” also enabled large-scale production of high-quality atom-thick nanosheets with controllable thicknesses<sup>16</sup> (**Fig. 2a**). Electrochemical exfoliation, using tetrahexylammonium cations ( $\text{THA}^+$ ) in tetraethylammonium bromide in N,N-dimethylformamide (DMF) electrolyte, provided a scalable approach to generating atom-thick InSe layers with precise structural control with the expression as below<sup>16</sup>:



Upon applied field,  $\text{THA}^+$  intercalates into the mother crystal bulk-InSe and expands the structure gradually through the intercalation. This eventually results in the production of InSe nanosheets. On the other hand,  $\text{Br}^-$  ions are reduced on the anode. Importantly, under an external electric field, biaxial tension strain induced by the electrochemical process can cause atomic distortion in  $\beta$ -InSe, breaking its inversion symmetry and transitioning it to a non-centrosymmetric structure. This distortion enables the emergence of both IP and OOP ferroelectricity in InSe<sup>16</sup>, indicating the structural and electrical properties are highly depending on the method.

Recently, to obtain high-quality 2D monolayers of InSe, the electrochemical molecular intercalation of  $\text{THA}^+$  was successfully achieved under the oxygen-free ambient<sup>84</sup>. The

electrochemical intercalation and exfoliation process were conducted within a N<sub>2</sub>-filed glovebox with oxygen and water levels below 1 ppm. Furthermore, acetonitrile and DMF were purged with N<sub>2</sub> and dried using molecular sieves to remove dissolved oxygen and residual moisture. The resultant InSe monolayers exhibited high purity and uniformity across the 4-inch wafer, while proving its high electrical properties, i.e., an average electron mobility of ~90-120 cm<sup>2</sup>/V·s, on-off ratio of ~10<sup>7</sup> in their transistors<sup>84</sup>.

For In<sub>2</sub>Se<sub>3</sub>, molecular intercalation with THA cations was applied with the exfoliation efficiency higher than 83 %, producing sheets up to 30 μm<sup>85</sup>. Furthermore, to the best of our knowledge, there are no reported cases of In<sub>2</sub>Se<sub>3</sub> exhibiting ferroelectric properties through liquid-phase processes. Therefore, minimizing the risk of degradation during the liquid-phase process is crucial for future large-scale production. Note that intercalation of alkali metals (e.g., Li, K, etc.) has not been demonstrated for InSe and In<sub>2</sub>Se<sub>3</sub> probably due to the charge transfer-induced degradation issues.

### ***Thin film growth***

Compared with mechanical/chemical exfoliation, thin-film growth of 2D materials offers key advantages for semiconductor industrial applications including thickness and stoichiometry control, enhanced potential for scale-up, gas-phase doping, uniformity across large areas, and the ability to tailor material properties by adjusting growth parameters. However, as indicated earlier, the polymorphic nature of the In-Se system complicates the synthesis of phase-pure and stoichiometric InSe or In<sub>2</sub>Se<sub>3</sub> films. During chemical vapor-based processes, a Se-rich environment typically favors the formation of In<sub>2</sub>Se<sub>3</sub>, while an In-rich condition increases the possibility of producing InSe<sup>12</sup>. Therefore, to achieve the desired stoichiometric composition, precise control over the flux of each precursor (i.e., chalcogen-to-metal ratio) is essential during the growth. Furthermore, the growth temperature and cooling rate also affect the crystalline phases and stacking orders, indicating that multiple growth parameters should be optimized to obtain reliable growth windows.

Metal-organic chemical vapor deposition (MOCVD) emerges as a promising technique for this purpose, particularly in comparison to powder-based thermal CVD (**Fig. 2b, c**). **Table 2** summarizes the melting and boiling points of precursors used in vapor-phase growth methods for indium selenides, alongside those for other representative group-VI 2D TMDs. Notably, MO sources, such as In(CH<sub>3</sub>)<sub>3</sub>, have lower melting points than metal or metal oxide

sources (In or In<sub>2</sub>O<sub>3</sub>). This lower melting point facilitates improved control of the sources, particularly because MOCVD utilizes a bubbler system equipped with electrical pressure controllers (EPCs) and mass flow controllers (MFCs), enabling precise regulation of the vapor pressure (**Fig. 2c**). It is also worth noting that group-III metal precursors, such as In, TMIIn, Ga and TMGa, exhibit significantly lower evaporation or sublimation temperatures than Group-VI transition metal precursors (e.g., Mo, W) (**Table 2**). For instance, In(CH<sub>3</sub>)<sub>3</sub> has a melting point of 88 °C, and Ga(CH<sub>3</sub>)<sub>3</sub> is in a liquid state at room temperature, whereas W has an exceptionally high melting point of 3,422 °C. This lower temperature requirement for group-III precursors thus provides a significant advantage for CMOS back-end-of-line (BEOL) integration at low temperatures (< 450-550 °C)<sup>86</sup> (the comparisons of preparation temperatures and grain (crystal) sizes depending on the methods are summarized in **Fig. 2e**).

**Table 2. Melting or boiling points of precursors for (MO)CVD of 2D TMDs or group-III metal chalcogenides**

	Precursors	Melting temp.
Group-VI transition metal precursors	Mo	2,623 °C
	MoO <sub>3</sub>	795 °C
	Mo(CO) <sub>6</sub>	150 °C
	W	3,422 °C
	WO <sub>3</sub>	1,473 °C
	W(CO) <sub>6</sub>	170 °C
Group-III metal precursors	In	157 °C
	InI	365 °C
	In(CH <sub>3</sub> ) <sub>3</sub>	88 °C
	In <sub>2</sub> O <sub>3</sub>	1,910 °C
	Ga	29.8 °C
	Ga(CH <sub>3</sub> ) <sub>3</sub>	-15.7 °C
	Ga <sub>2</sub> O <sub>3</sub>	1793 °C
Chalcogen precursors	S	120 °C
	Se	221 °C
		*Boiling temp.
	(CH <sub>3</sub> ) <sub>2</sub> S	37.33 °C*
	(C <sub>2</sub> H <sub>5</sub> ) <sub>2</sub> S	92.1 °C*
	(CH <sub>3</sub> ) <sub>2</sub> Se	49.8 °C*

We also compare the various growth techniques for group-III metal chalcogenides, (e.g., InSe, In<sub>2</sub>Se<sub>3</sub>, GaSe and Ga<sub>2</sub>Se<sub>3</sub>), including molecular beam epitaxy (MBE)<sup>87-89</sup>, physical vapor deposition (PVD)<sup>55,90-92</sup>, thermal CVD<sup>13,93,94</sup>, and MOCVD<sup>12,95</sup>. Thermal CVD is the most widely adopted method due to its easy accessibility, and it can grow relatively large grain sizes (~10–100 μm) with moderate growth rates (several nm/min) by manipulating solid-state precursors (e.g., In<sub>2</sub>O<sub>3</sub> and Se powders) (**Fig. 2f**). However, sublimation of the sources requires high growth temperatures (700–900°C), while challenging precise control of the metal-to-chalcogen ratio. Hence, powder-based CVD of stoichiometric InSe remains difficult, with only two related reports available<sup>93,94</sup>. Chemical vapor transport (CVT), which employs InSe source powder and NH<sub>4</sub>Cl as a transport agent within a sealed quartz tube, also enables the growth of few-layer InSe or In<sub>2</sub>Se<sub>3</sub>, depending on growth temperatures (~400°C or ~450°C, respectively)<sup>96</sup>. High-quality In<sub>2</sub>Se<sub>3</sub> can also be obtained by PVD (or quasi-equilibrium growth<sup>90</sup>) using In<sub>2</sub>Se<sub>3</sub> powder at high temperatures (~850 °C)<sup>55,90-92</sup>; still, PVD of InSe is challenging due to the lack of controllability over In-to-Se ratio. In addition, both CVT<sup>96</sup> and PVD<sup>55,91,92</sup> typically produce randomly oriented few-layer flakes with smaller grain sizes (< 20 μm) and lack scalability and thickness controllability. In contrast, MOCVD presents a promising approach for scalable and high-quality InSe or In<sub>2</sub>Se<sub>3</sub> production, offering epitaxial mode, wafer-scale growth, moderate growth temperatures (~400-500°C), and thickness controllability<sup>12,95</sup> (**Fig. 2f**). While MBE can similarly achieve large-scale, thickness-controlled InSe or In<sub>2</sub>Se<sub>3</sub> by adjusting growth temperature and source flux ratio<sup>87-89</sup> (**Fig. 2d**), its limited throughput for producing large-area thin films and cost aspects (for maintaining ultra-high vacuum to 10<sup>-10</sup> torr, etc) restrict its commercialization when compared with MOCVD.

Despite recent advancements in growth techniques, the electrical performance of synthesized indium selenide films still lags behind that of mechanically exfoliated (labeled as “ME” in **Fig. 2g**). Specifically, the field-effect mobility of (MO)CVD-grown InSe films (typically ~1–10 cm<sup>2</sup>/V·s) is significantly lower than their mechanically exfoliated counterparts (~10<sup>3</sup> cm<sup>2</sup>/V·s of Hall mobility for InSe flakes with the thickness of ~5 nm). This reduced mobility in synthetic films is largely attributed to defects such as undesired oxides, vacancies, grain boundaries, and phase impurities, which hinder charge carrier transport. Consequently, there is a pressing need for improved growth methods aimed at minimizing defects, and enhancing crystal quality. One promising approach involves the use of flow-modulation MOCVD to optimize the ripening stage, thereby reducing nucleation densities and promoting lateral growth<sup>12</sup>. Additionally, unidirectionally oriented epitaxial growth—similar to recent

advances in the epitaxial growth of wafer-scale group-VI TMDs single crystals<sup>97</sup>—holds potential for producing high-quality thin films, given the fact that step-edge-guided nucleation and growth of InSe or In<sub>2</sub>Se<sub>3</sub> on a vicinal-stepped substrate (e.g., sapphire with an off-cut angle) has yet to be observed.

Therefore, future efforts should focus on developing epitaxial growth strategies with precise control over nucleation and domain alignment, potentially utilizing stepped substrates with controlled miscut angles to guide crystal orientation. Implementation of advanced in-situ characterization techniques during growth could enable real-time monitoring of phase formation, potentially allowing for automated feedback systems that dynamically adjust growth parameters to maintain stoichiometric control across entire wafers. The integration of machine learning approaches for optimizing the complex growth parameter space—including temperature, precursor ratios, and flow modulation patterns—holds promise for rapidly identifying conditions that maximize mobility while minimizing defect density. Finally, developing low-temperature growth processes (<450°C) compatible with CMOS back-end-of-line requirements will be essential for enabling heterogeneous integration of indium selenide devices with silicon technology, potentially offering a pragmatic path toward commercial implementation.

### ***Mitigation of surface oxidation***

As predicted by the In-Se-O phase diagram, indium selenides can undergo oxidation to finally form In<sub>2</sub>O<sub>3</sub> and In<sub>2</sub>(SeO<sub>4</sub>)<sub>3</sub>. According to multiple studies, when ultrathin InSe is exposed to pure oxygen or air at room temperature, p-type doping and current hysteresis behaviors can arise<sup>98,99</sup>, making it difficult to achieve the desired high conductivity in transistor applications. Furthermore, it has been reported that the oxidative behavior of InSe depends on the degree of defects (such as Se vacancies)<sup>100</sup> and on its thickness<sup>79</sup>. In the case of In<sub>2</sub>Se<sub>3</sub>, exposure to oxygen and moisture can induce the formation of an amorphous In<sub>2</sub>Se<sub>3-3x</sub>O<sub>3x</sub> surface layer, a process that is further accelerated under light illumination. One study in 2023 revealed that once this oxidation takes place, Se hemisphere particles may form on the oxidized In<sub>2</sub>Se<sub>3-3x</sub>O<sub>3x</sub> surface<sup>101</sup>. Notably, the oxidation characteristics depend on the surface coordination environment: octahedral coordination of atoms in both  $\alpha$  and  $\beta$  phases is less stable than tetrahedral coordination in  $\alpha$  phase, thereby facilitating the formation of these Se particles<sup>101</sup>.



On the other hand, the resultant  $\text{In}_2\text{Se}_{3-3x}\text{O}_{3x}$  layer can self-passivate the surface by limiting oxidation to just a few nanometers in thickness, suggesting that thicker  $\text{In}_2\text{Se}_3$  may exhibit reduced oxidation<sup>101</sup>.

Consequently, optimizing their surface chemistry and developing protective coatings that preserve their electronic properties are imperative for large-scale adoption of indium selenides in electronic devices. The most widely used method to retard the oxidation of indium selenides involves fabricating encapsulation layers (e.g.,  $\text{HfO}_2$ ) by atomic layer deposition, which effectively isolates the crystals from moisture and oxygen in the environment and improve its stability<sup>10</sup>. One can also conduct dry oxidation to form a nonstoichiometric, self-limiting  $\text{InSe}_{1-x}\text{O}_x$  oxide layer<sup>79</sup>. The formation of dry oxide layer retards further oxidation of the underlying  $\text{InSe}$ , thereby enabling a high two-probe field-effect mobility ( $>450 \text{ cm}^2\text{V}^{-1}\text{s}^{-1}$  at 300 K for 13-nm-thick  $\text{InSe}$ ) in its FET<sup>79</sup>. For device fabrication, it is essential to use an air-stable fabrication method compatible with photo-beam or electron-beam lithography. It has been reported that baking the e-beam resists at a lower temperature (e.g., 110 °C) than usual (e.g.,  $> 180 \text{ °C}$ ) in a vacuum, and then quickly placing it in a high-vacuum environment, helps minimize the formation of free radicals that degrade  $\text{InSe}$  contact interface<sup>10</sup>. Nevertheless, more fundamental investigations into kinetics, mechanisms, and possible prevention strategies for oxidation are needed to provide valuable insights that guide the design of more robust, indium selenides-based applications.

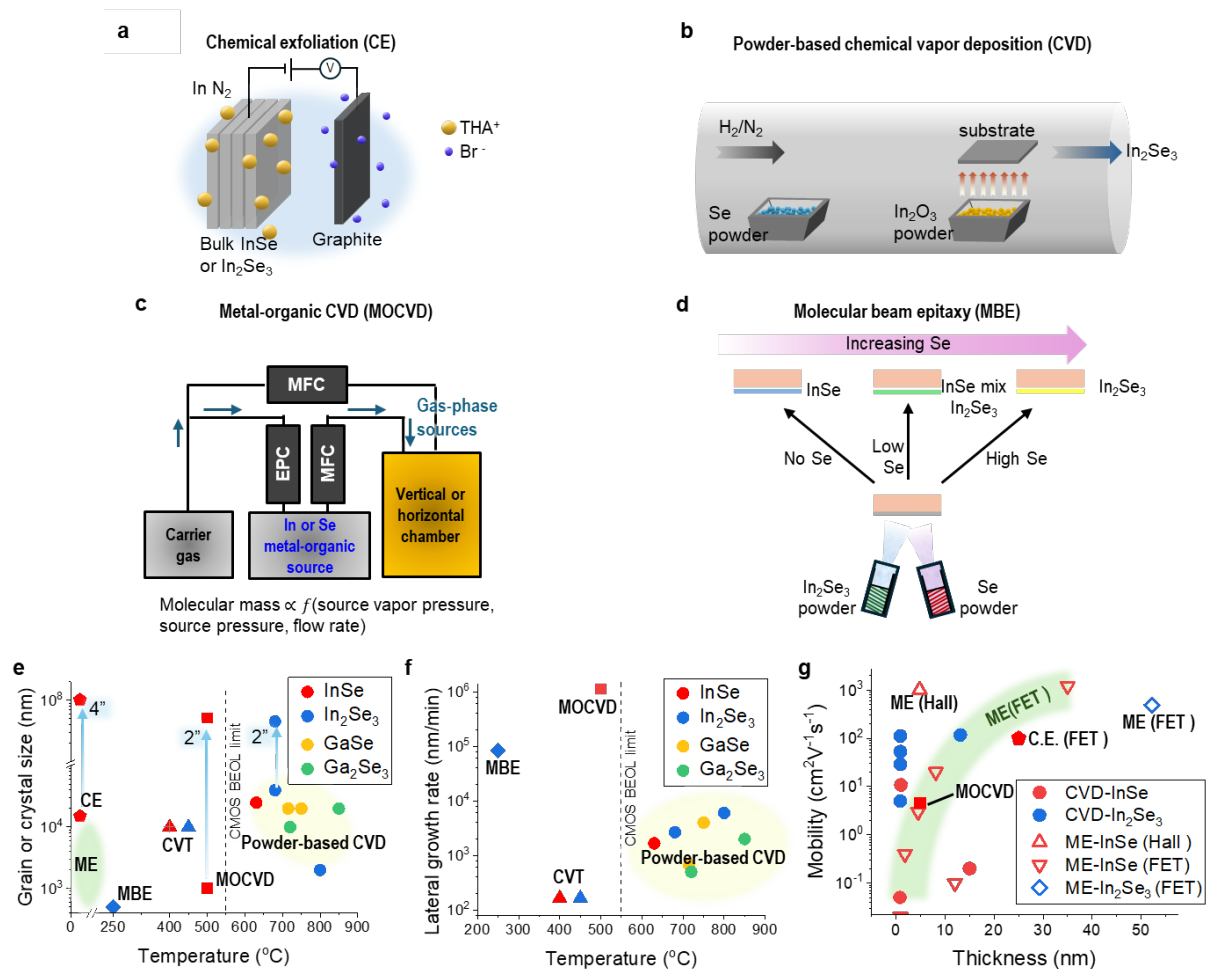


**Figure 2. Various production methods for van der Waals III-VI compound semiconductors.** (a-d) Schematics of different preparation methods of indium selenides; (a) chemical exfoliation (CE), (b) powder-based chemical vapor deposition (CVD), (c) metal-organic CVD (MOCVD), and (e) molecular beam epitaxy (MBE). (e,f) Relationship between production temperatures and (e) grain size or exfoliated crystal size, and (f) lateral growth rate across various growth or production techniques reported in the literature, including mechanical exfoliation (ME), CE, power-based CVD<sup>102-108</sup>, chemical vapor transport (CVT)<sup>96</sup>, MBE<sup>87</sup>, and MOCVD<sup>12</sup>. The arrows in (e) indicate wafer-scale production of the thin films. (g) Thickness-dependent Hall or field-effect mobility of InSe and In<sub>2</sub>Se<sub>3</sub> produced by (MO)CVD and CE (solid) compared to ME samples (open).

## Low-Power Transistor Applications

Transistors are fundamental and critical components in modern electronics, driving the research community and semiconductor industries for decades. 2D semiconductors offer an exciting path toward transistor scaling beyond the conventional 5 nm node. Their atomic-scale thickness of a few nm greatly improves electrostatic control, which makes them promising for physical sub-10 nm gate lengths. 2D channels have dangling-bond-free surfaces that reduce interface traps and variability, and they can be integrated in 3D device architecture (e.g., vertically stacked nanosheet or nanowire FETs) for enhanced drive current and higher device density. Even with its simple planar structure, a metal-oxide semiconductor FET (MOSFET) using a 2D semiconductor channel (**Fig. 3a**) demonstrates the potential to eventually replace conventional Si channels<sup>4,109,110</sup>. Nevertheless, major hurdles remain, including finding the most viable channel material options among the versatile 2D semiconductors. In this regard, InSe stands out as a promising material for logic device fabrication due to its exceptional electronic properties, including high carrier mobility, low thermal conductivity, and ballistic transport.

Beyond conventional thermionic MOSFET operation, 2D semiconductors also enable novel “steep-slope” device concepts that can reduce the switching power below the limit of traditional FETs by overcoming the  $\sim 60$  mV/dec subthreshold slope (SS) limit at room temperature. Their exceptionally high carrier mobility makes 2D semiconductors particularly appealing for these emerging steep-slope transistors, while their van der Waals surfaces and easy integration offer extensive opportunities for band engineering and device design. For example, in tunneling FETs (TFETs), 2D heterojunctions with type-III band alignment can promote band-to-band carrier tunneling and facilitate sub-thermionic ( $< \sim 60$  mV/dec) switching, albeit with ongoing challenges in boosting the on-state current. These breakthroughs suggest that high-mobility 2D semiconductors, when combined with advanced device physics approaches (e.g., tunneling) and 3D integration, could be key to continuing transistor scaling and enabling ultra-low-power operation in next-generation electronics. In this section, we discuss these advancements, with particular emphasis on the potential of InSe-based FETs for future low-power logic applications. Furthermore, InSe FET as an excellent platform for investigating new electrical and optical properties are reviewed.

### ***Ballistic InSe FETs and high thermal velocity (mobility).***

The most attractive feature of InSe for electronic applications is the high electron mobility. Even early (non-optimized) InSe transistors exhibit mobilities higher than what is currently achievable with single crystal TMDs<sup>111-113</sup>. Rapid improvement of InSe transistor performance has been made by employing smooth PMMA substrates<sup>8,114,115</sup>, passivation by controlled oxidation<sup>79,116,117</sup>, indium capping<sup>118</sup>, and encapsulation with hBN<sup>6,119-121</sup>. Room temperature field effect mobilities in these devices can routinely exceed  $1,000 \text{ cm}^2\text{V}^{-1}\text{s}^{-1}$ ; competing with state-of-the-art silicon transistors<sup>6,8,114,118,121</sup>.

This high mobility of InSe could be achieved attributed to exceptionally high thermal velocity,  $\sim 2 \times 10^7 \text{ cm/s}$ <sup>122</sup>, which exceeds that of all semiconducting TMDs and silicon at equivalent thicknesses (**Fig. 1d**). This high thermal velocity enables electrons to travel through the transistor channel with minimal scattering when the channel length is short enough and ohmic contact exists. As a result, carriers traverse the channel without undergoing significant scattering with phonons or impurities, preserving their energy and momentum, which is critical for reducing power dissipation and ensuring faster operation (**Fig. 3b**). This is important because, at ultra-short channel lengths, 2D material FETs are typically limited by the thermal velocity of the channel material—determined solely by the material’s effective electron mass<sup>11,34,35</sup>. Due to its small effective mass ( $\sim 0.1m_0$ ) down to monolayer thickness, the thermal velocity of InSe exceeds that of all semiconducting TMDs as well as silicon at equivalent thicknesses.

Recently, by employing contact engineering, encapsulation with high-k dielectric, and scaled channel lengths ( $< 20 \text{ nm}$ ), ballistic transistors utilizing 2.4 nm-thick InSe have been demonstrated<sup>10</sup>. The device, with a 10 nm channel length, achieves ohmic contacts through Y-doping-induced phase transitions in InSe. By minimizing phonon scattering and leveraging its high thermal velocity, InSe ballistic transistors offer significant potential for low-power, energy-efficient computing, making them a promising material for next-generation electronic devices. When compared to other 2D material-based devices and conventional semiconductor-based transistors, the ballistic InSe transistor demonstrates exceptional transfer characteristics, including a SS of  $\sim 75 \text{ mV/dec}$  (**Fig. 3i, j**) and a record-high transconductance of 6 mS (**Fig. 3j**). These impressive benchmarks suggest that InSe holds considerable promise for high-performance transistor fabrication, potentially competing with MoS<sub>2</sub> or Si-based FETs.

However, further investigation is required to better understand aspects like reliability and manufacturability, and a more detailed comparison would provide a clearer perspective.

### ***Flat bands of InSe and its detection in FETs***

In addition, InSe FETs provide an excellent platform for studying new physical properties of 2D InSe. One notable discovery involves detecting InSe's flat band (a van Hove singularity near the valence band) through electrical measurements<sup>123</sup> (**Fig. 3e, f**). The measurement of the flat band can be conducted using a FET with a simple but effective design: it is sandwiched InSe between two hBN insulating layers and used graphene for the source and drain contacts (**Fig. 3e**). By adjusting the gate voltage ( $V_G$ ), one can move InSe's Fermi level from the conduction band, through the bandgap, and into the valence band region. Hence, out-of-plane tunneling current using carriers generated by visible laser light can be measured. When the Fermi level reaches the van Hove singularity near the valence band (blue line in **Fig. 3f**), the density of states increases sharply, causing a distinct spike in tunneling current. This effect becomes particularly noticeable as the tunneling mechanism shifts from direct to Fowler-Nordheim tunneling at the flat band. Compared to traditional measurement techniques like ARPES or STM/ST-spectroscopy (STM/STS), this electrical detection method is remarkably simple<sup>123</sup>. Since flat bands typically exhibit large effective masses and strong electron-electron interactions, InSe might display interesting phenomena like magnetic and superconducting phase transitions. Additionally, the transistor structure enables studying spin polarization and chirality effects in 2D InSe by measuring photo-excited holes tunneling through the hBN barrier under magnetic fields.<sup>125</sup>

### ***Ballistic avalanche InSe/BP heterojunction FETs.***

By leveraging InSe's superior electron mobility, ballistic transport characteristics, and van der Waals properties, one can form heterostructures composed of InSe and other 2D or 3D semiconductors (**Fig. 3c, g**). Depending on how carriers transport across these semiconductors, such heterostructures can be utilized in devices such as impact ionization transistors or tunneling transistors.

For instance, by using InSe as an n-type semiconductor and BP as a p-type

semiconductor, both electrons and holes can be sufficiently accelerated within the heterostructure to drive impact ionization<sup>124</sup> (**Fig. 3g, h**). As a result, unlike the conventional impact ionization (avalanche) phenomenon seen in bulk semiconductors, a ballistic avalanche phenomenon can be observed in vertical InSe/BP heterostructures. While typical avalanche devices require high voltages in the order of tens of volts or a long impact ionization region, this study demonstrates avalanche breakdown at voltages below  $\sim 1$  V. Moreover, the devices exhibit excellent noise performance and enable the realization of transistors with extremely low subthreshold swings, as well as high-sensitivity avalanche photodetectors (APDs).

### ***Tunnel FETs based on InSe/Si heterojunction.***

Miao et al. demonstrated an TFET composed of 2D InSe and 3D Si (**Fig. 3c**), exhibiting sub-60 mV/decade operation, an on-state current density of  $\sim 0.3 \mu\text{A}/\mu\text{m}$ , and an on/off current ratio of  $\sim 10^6$ . These remarkable results are attributed to the type-III band alignment formed between InSe and Si, which establishes an optimal offset in their conduction and valence bands. Moreover, the atomic-scale thickness of InSe not only maximizes gate electrostatic control but also, owing to its van der Waals surface, provides the clean and thin channel essential for TFETs. Consequently, when suitable gate and drain voltages are applied, band-to-band tunneling is readily induced.

As shown in the benchmarking results in **Fig. 3i** and **3j**, the subthreshold swing of InSe TFETs is comparable to that of BP-based TFETs and superior to that of 3D InAs-based TFETs. However, the current density of InSe TFET ( $< 1 \text{ mA}/\mu\text{m}$ ) is still lower than those of Si- or 2D semiconductor-based MOSFETs (**Fig 3j, k**). These characteristics suggest that InSe-based TFETs could be a competitive option for next-generation logic devices, as they combine the benefits of 2D material properties with excellent electrostatic control for efficient tunneling and switching performance; however, there is still substantial room for improvement in achieving high on-state conductance. Thus, it is necessary to find better material options for semiconductor with bandgap compatible with InSe, and to implement automated, large-area processes that can optimize characteristics of interfaces at junctions, contacts, and dielectrics.

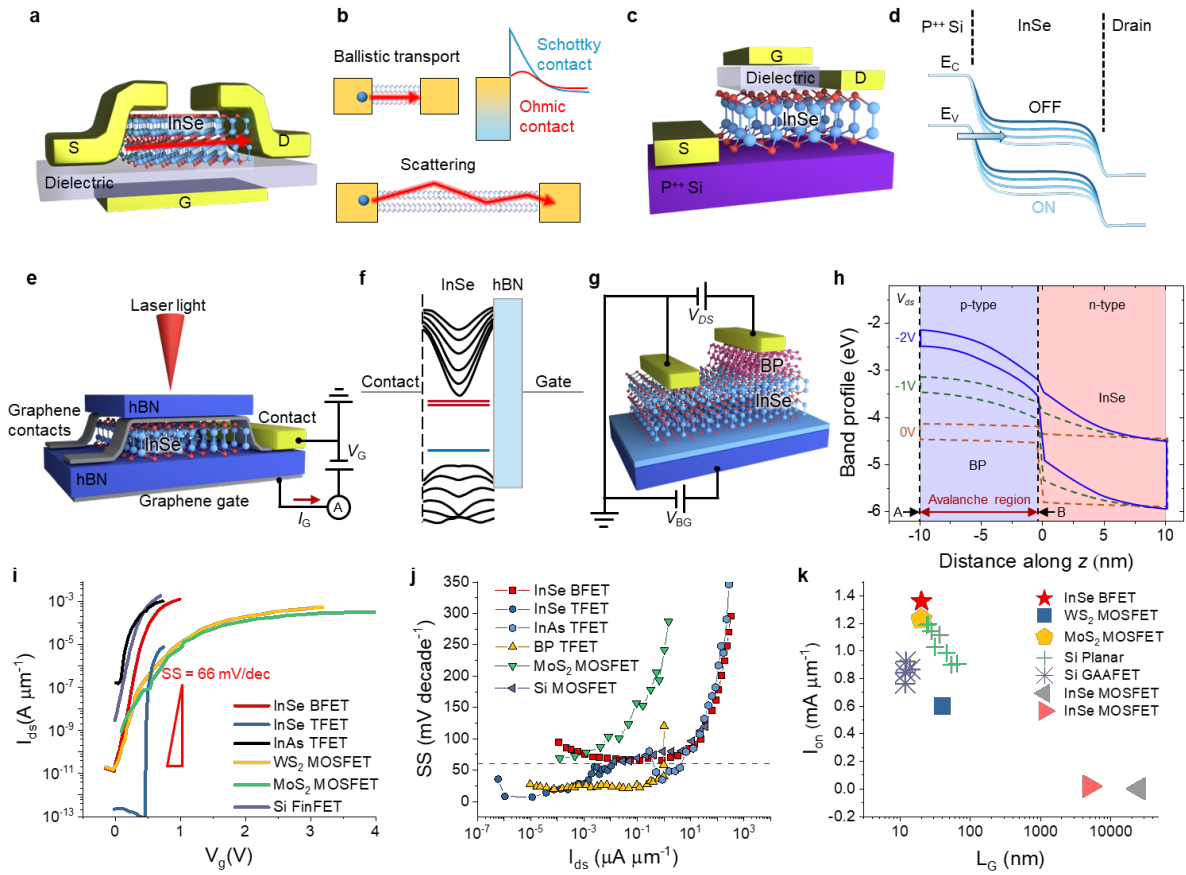


**Figure 3. Various transistors based on InSe.** (a,b) Ballistic field-effect transistor (FET) based on InSe. (a) Representative structure of InSe FET; (b) contact engineering to achieve ohmic contacts and short channel length are critical for realization of ballistic transport rather than scattering of carriers. (c, d) Tunneling field-effect transistor (TFET) utilizing InSe as the channel material; Schematics of (c) the devices structure, and (d) the working mechanism of band-to-band tunneling. (e, f) Observation of flat band in a FET; (e) Schematic of the InSe FET and proving the tunneling current through gate-source current ( $I_G$ ) under the laser illumination, and (f) band structure of InSe with flat bands (red and blue lines). (g,h) Ballistic avalanche phenomena in InSe heterojunction FETs; (g) device structure, and (h) band profile of the heterostructures. (i, j), Benchmarking plots of (i) transfer curves and (j) subthreshold swing (SS) in InSe-based FETs, that is, ballistic FET (BFET), TFET, metal-oxide-semiconductor FET with an oxide dielectric gate (MOSFET) and fin-shaped FET (FinFET), compared to various 2D materials and conventional semiconductor materials<sup>122,125,126</sup>. (k) On-state current density ( $I_{on}$ ) depending on channel lengths ( $L_G$ ) of InSe-based devices and their comparisons with other Si or 2D material-based transistors<sup>122,125,126</sup>.

## Non-Volatile Memory Device Applications

Ferroelectricity in 2D materials have attracted significant research interest due to its potential applications in energy-efficient computing platforms, when applying the non-volatile properties of the ferroelectric polarizations<sup>127</sup>. When coupled with the van der Waals nature of 2D materials, in particular, ferroelectricity offers an innovative approach to address challenges faced by traditional 3D ferroelectrics, such as scaling limitations and performance degradation at reduced thicknesses<sup>15,127,128</sup>. Moreover, van der Waals layered InSe and In<sub>2</sub>Se<sub>3</sub>, even with their atomic-scale thickness and a bandgap of > 1.41 eV, exhibit either sliding ferroelectricity or spontaneous ferroelectricity despite not being insulators. This enables the integration of strong polarization responses with functionalities derived from their semiconducting properties, facilitating the development of compact, energy-efficient devices for in-memory, in-sensory computing, neuromorphic systems, and optoelectronics<sup>15,127,128</sup>. Their unique van der Waals structure provides a significant advantage, characterized by the weak interlayer coupling and fewer dangling bonds at the surfaces, which substantially reduces interfacial defect formation in ferroelectric devices. Furthermore, the high Curie temperature of In<sub>2</sub>Se<sub>3</sub> makes it especially attractive as it allows for maintaining stable operation under high temperatures generated by Joule heating. Altogether, InSe and In<sub>2</sub>Se<sub>3</sub> as 2D ferroelectric semiconductors have emerged as compelling candidates for next-generation memory devices. In this subsection, therefore, we review InSe and In<sub>2</sub>Se<sub>3</sub> applied to ferroelectric tunnel junctions (FTJs)<sup>20,42,129-132</sup> and ferroelectric semiconductor FETs (FeSFETs)<sup>19,133-136</sup>, and assess their potential for future ultra-high-density, low-power memory applications.

### In<sub>2</sub>Se<sub>3</sub> ferroelectric tunneling junctions

FTJs are next-generation memory devices that utilize electron tunneling through an ultrathin ferroelectric film, exhibiting nonvolatile resistance changes depending on the polarization orientation. A typical FTJ adopts a metal–ferroelectric–metal (MFM) configuration, in which a nanometer-thick ferroelectric layer serves as the tunneling barrier, and is sandwiched between two metals electrodes, and metallic oxide or semiconducting interlayer is sometimes inserted between metal and ferroelectric (**Fig. 4a**). In this structure, electrons tunnel quantum-mechanically through the ferroelectric barrier, and the reversal of ferroelectric polarization shifts the barrier height and/or width, thereby altering the tunneling current in a nonvolatile manner. This phenomenon, referred to as tunneling electroresistance (TER), is quantified by



its on-off ratio, which is a key figure of merit for FTJ memory operation. FTJs are emerging as a next-generation high-speed, low-power non-volatile memory that can replace or complement existing FeRAM, NAND flash, and MRAM technologies. Several FTJs also show significant potential for multi-state applications and as an analog synaptic device.

For  $\text{In}_2\text{Se}_3$ , ferroelectric properties can be maintained down to the thickness of a two-dimensional material monolayer, and TER characteristics of over  $10^4$  have been observed in various  $\text{In}_2\text{Se}_3$  FTJs<sup>20,131,132</sup>. Contributed from van der Waals stacking of different materials, the FTJ structures of metal/interlayer/ $\alpha$ - $\text{In}_2\text{Se}_3$ /p+Si<sup>20</sup>, metal/h-BN/ $\alpha$ - $\text{In}_2\text{Se}_3$ /graphene<sup>131</sup>, metal/ $\alpha$ - $\text{In}_2\text{Se}_3$ /MoS<sub>2</sub><sup>132</sup> have been proposed. The interlayer provides asymmetry of the band alignment, while modulating effective Schottky barrier height<sup>20,131,132</sup> and suppressing the thermionic current leakage to obtain pure TER mechanisms<sup>132</sup> (**Fig. 4b**). In particular, the metal/ $\alpha$ - $\text{In}_2\text{Se}_3$ /MoS<sub>2</sub><sup>132</sup> FTJs exhibit both room-temperature negative differential resistance (NDR) effect and high tunnel TER exceeding  $10^4$  simultaneously, while providing temperature independence of the transport. Recently, ferroelectric van der Waals metal of WTe<sub>2</sub> has been used as metal electrode for  $\text{In}_2\text{Se}_3$  FTJs (i.e., WTe<sub>2</sub>/ $\alpha$ - $\text{In}_2\text{Se}_3$ /metal)<sup>137</sup>. The use of WTe<sub>2</sub> allows for the high on-off ratio of  $10^5$ , with the switching voltage less than 2 V. In addition, the multiple resistance levels have been observed due to the pinning effect of the WTe<sub>2</sub>/ $\alpha$ - $\text{In}_2\text{Se}_3$  interface on the upward polarization of  $\alpha$ - $\text{In}_2\text{Se}_3$ . This permits the polarization of  $\alpha$ - $\text{In}_2\text{Se}_3$  to maintain a partially switched polarization state, resulting in an intermediate resistance level. Besides, the atomic configurations (i.e., 2H or 3R stacking) of  $\alpha$ - $\text{In}_2\text{Se}_3$  influence the polarization switching mechanism and the TER effect<sup>42</sup>, highlighting the importance of phase-pure material preparation to achieve the desired properties. Furthermore, future advancements in controlling high on-off ratios appear promising through strategic manipulation of the tunneling barrier. This can be realized by employing a range of physical and chemical techniques, including precise optimization of interfacial characteristics and strategic modulation of the interfacial barrier.

Despite this potential, however, an on-off ratio of  $\text{In}_2\text{Se}_3$  FTJ<sup>20,42,129-132</sup> is currently limited to  $\sim 10^5$ , which is relatively lower compared to other FTJs. For instance, the state-of-the-art bulk ferroelectric-based FTJ (e.g., Pt/BTO/NbSTO) exhibits an on-off ratio of  $\sim 10^8$  (ref.<sup>138</sup>), and the van der Waals ferroelectric CuInP<sub>2</sub>S<sub>6</sub> (CIPS)-based FTJ achieves  $\sim 10^{10}$  at RT (ref.<sup>139</sup>), both significantly higher than that of  $\text{In}_2\text{Se}_3$  FTJ<sup>20,42,129-132</sup> (**Fig. 4e**). Moreover, there have been no studies to date demonstrating the analog synaptic behavior in  $\text{In}_2\text{Se}_3$  FTJ by

controlling the degree of partial ferroelectric domain switching through variations in voltage pulse magnitude or pulse width. More importantly, there remain significant challenges for the integration of  $\text{In}_2\text{Se}_3$  FTJs into crossbar array devices within CMOS BEOL-compatible fabrication processes and large-scale integration technologies. Therefore, addressing the inherent issues of  $\text{In}_2\text{Se}_3$  production processes (e.g., high temperature, wafer-scale uniformity and precise thickness control) is essential for future developments.

### **InSe and $\text{In}_2\text{Se}_3$ ferroelectric semiconductor FETs**

Compared with two-terminal FTJs, three-terminal ferroelectric FETs (FeFETs) offer multiple advantages in terms of operating mechanism and practical utility<sup>140</sup>. For instance, two-terminal ferroelectric devices typically ascertain the memory state by applying voltage and measuring the resulting current, which can lead to destructive readout if the polarization is altered or partially lost during measurement<sup>141</sup>. In contrast, in a three-terminal FeFET architecture, one can measure the channel doping state indirectly by simply adjusting the gate voltage, thus enabling non-destructive readout<sup>140,142</sup>. Because the read and write pathways are physically separated, these transistor-based devices provide higher device stability and better data retention. Additionally, the channel conductivity is modulated through the gate, while ferroelectric polarization maintains non-volatility, making it more straightforward to combine logic and memory functionality within a single device<sup>143</sup>. In other words, FeFETs are well suited for next-generation non-volatile memories, neuromorphic computing, and logic-in-memory applications, thanks to their fast-switching characteristics, potential for high-density integration, and low power consumption. By finely tuning the gate voltage, these devices can realize multi-level channel current control, synaptic weight updates, and independent readout signals.

In the case of InSe and  $\text{In}_2\text{Se}_3$ , both materials can exhibit ferroelectric behavior yet have a relatively small bandgap ( $> 1.41$  eV) compared with bulk ferroelectric insulators. This property has attracted attention for potential applications as “ferroelectric semiconductor FETs” (FeSFETs)<sup>19,133-136</sup> (**Fig. 4c**). Unlike conventional three-terminal FeFETs that use a ferroelectric layer as the gate dielectric, InSe and  $\text{In}_2\text{Se}_3$  allow the use of a standard gate dielectric while still enabling polarization control in the channel. Because the channel itself is ferroelectric, reorienting the polarization critically alters the channel doping concentration and conductivity (**Fig. 4d**). Depending on the effective oxide thickness (EOT), different portions of the channel’s

top or bottom surfaces may be polarized, and the electric field may penetrate to varying depths<sup>19</sup>. Consequently, the transfer characteristics can exhibit clockwise or counterclockwise hysteresis (that is, a memory window), and because this polarization is preserved even when power is removed, these transistors can serve as non-volatile memory that integrate logic and memory in a single device.

In conventional FeFETs employing a bulk ferroelectric gate, incomplete screening of polarization along the channel can degrade memory properties<sup>144</sup>. In contrast, InSe and In<sub>2</sub>Se<sub>3</sub> channels can screen the polarization charges internally, reducing gate-interface trapping and leakage, thus improving retention<sup>19,127</sup>. Additionally, thin-film ferroelectric gate oxides can introduce polycrystalline grains and interfacial complexities, but van der Waals 2D materials such as InSe and In<sub>2</sub>Se<sub>3</sub> typically experience fewer degradation pathways. Their ultrathin channels also simplify threshold voltage control and facilitate device scaling, offering advantages for highly integrated, low-power electronics. Compared with other 2D ferroelectric materials (e.g., CuInP<sub>2</sub>S<sub>6</sub><sup>73,145</sup>, SnS<sup>146</sup>), InSe and In<sub>2</sub>Se<sub>3</sub> provide a suitable bandgap (> 1.41 eV), higher carrier mobility (> 100 cm<sup>2</sup>V<sup>-1</sup>s<sup>-1</sup>), and stable ferroelectricity at room temperature (see also comparisons of remnant polarizations and coercive fields in **Fig. 1f** and **Table 2**).

Similar to prior FeFET studies, these 2D InSe and In<sub>2</sub>Se<sub>3</sub> FeSFETs can be driven analogously by controlling the polarization charge via the gate, enabling multi-bit storage and synaptic weight updates<sup>147-150</sup>. They also show rapid write/erase speeds and can operate under sub-microsecond or even nanosecond pulses, making them highly promising for high-speed neuromorphic computation. Simply switching the channel's polarization can integrate logic (e.g., AND, OR, NAND, NOR) and memory within a highly scalable architecture that overcomes the von Neumann bottleneck via on-chip in-memory computing.

Nevertheless, as discussed previously regarding the growth of InSe and In<sub>2</sub>Se<sub>3</sub> thin films, significant challenges remain in reproducibly achieving large-area, high-crystallinity layers at an industrial scale. Furthermore, device-level validation of interface stability, operating temperature ranges, and long-term endurance is also becoming increasingly important, given that current In<sub>2</sub>Se<sub>3</sub> FeSFETs<sup>133-136</sup> often show endurance ~10<sup>4</sup> cycles and retention on the order of 10<sup>5</sup> seconds (**Fig. 4f, g**). To ensure robust performance, it is essential to optimize selection of metal contacts and gate dielectrics to minimize contact resistance, trap states, and device degradation. In this regard, employing 2D ferroelectric metal contacts

(similar to work with  $WTe_2/\alpha\text{-In}_2\text{Se}_3/\text{metal}$  FTJ<sup>137</sup>) could open up further possibilities for developing reliable, high-performance ferroelectric semiconductor devices.

In addition, similar to a recent study on FeFETs based on sliding ferroelectricity of bilayer BN<sup>151</sup>, which demonstrated the endurance of  $> 10^{11}$  cycles, sliding ferroelectricity in InSe may offer enhanced robustness against fatigue; hence, further investigation is necessary. Conventional FeFETs tend to degrade due to defect formation at the ferroelectric/channel interface, leading to premature breakdown as well as reduced polarization and memory window<sup>152</sup>, whereas sliding ferroelectrics maintain high endurance through an in-plane sliding mechanism enabled by van der Waals bonding that minimizes the effects of defect formation<sup>151</sup>.

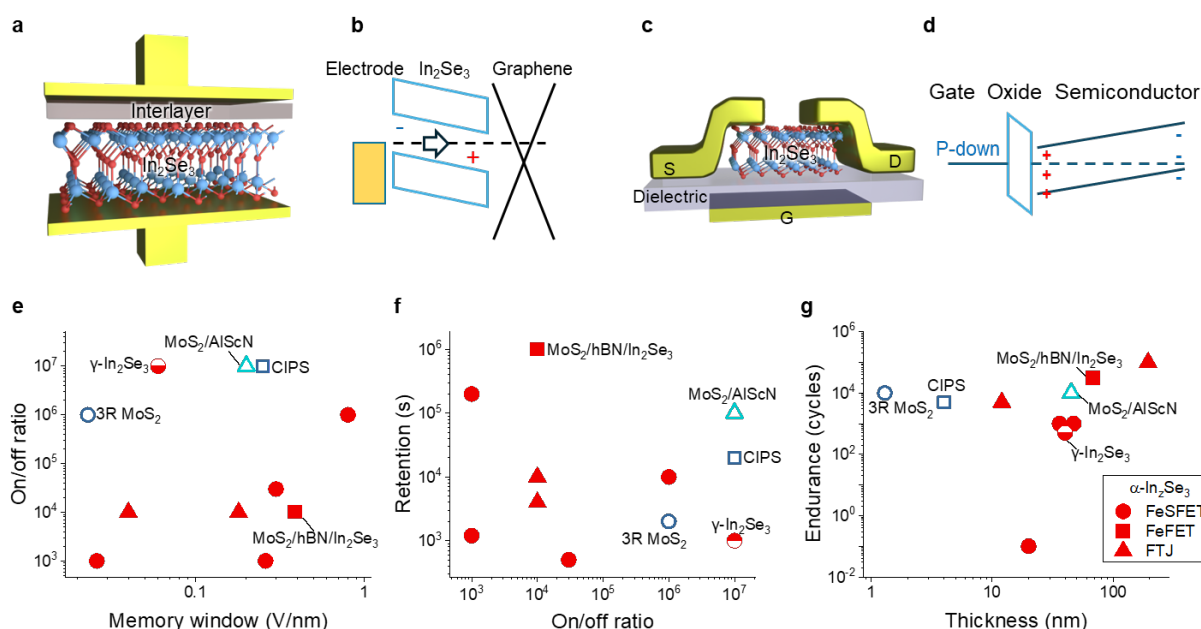


**Figure 4. Non-volatile ferroelectric memory devices based on  $\text{In}_2\text{Se}_3$**  (a), Schematic of an  $\text{In}_2\text{Se}_3$ -based ferroelectric tunneling junction (FTJ) device with an interlayer. (b) Schematic illustrating the working principle of a FTJ with a graphene interlayer. (c) Schematic of a ferroelectric semiconductor field-effect transistor (FeSFET) using  $\text{In}_2\text{Se}_3$ . (d) Schematic showing polarization-dependent operation in a FeSFET. (e) Benchmarking of on/off current ratio dependence on the memory window in  $\text{In}_2\text{Se}_3$  and other ferroelectric 2D materials. (f) Retention time vs. on/off ratio in  $\text{In}_2\text{Se}_3$  based ferroelectric devices. (g) Endurance depending on thickness of  $\text{In}_2\text{Se}_3$  and their comparisons with other ferroelectric devices with 2D materials<sup>129,130,133-136,153-157</sup>. The red solid symbols in (e-g) specifically represent electrical devices with  $\alpha$ -phase  $\text{In}_2\text{Se}_3$  channels: circles indicate FeSFETs, squares indicate FeFETs, and triangles indicate FTJs.

## Outlook

The development of van der Waals indium selenides for advanced logic and memory applications remains at an exciting early stage compared to established silicon and compound semiconductor technologies. Our analysis in this perspective suggests that indium selenides offer a unique pathway toward surpassing current materials while maintaining compatibility with existing semiconductor manufacturing infrastructure. For logic applications, InSe's exceptional carrier mobility and ballistic transport characteristics position it ideally for ultra-scaled transistors operating at the quantum limit. Future research should focus on optimizing contact resistance at scaled dimensions and developing reliable approaches to control doping in InSe channels. We anticipate that near-term advances in ballistic InSe transistors will likely appear first in specialized, high-performance computing applications where their superior switching energy and electrostatics can justify integration challenges. Full-scale commercial adoption will require significant progress in wafer-scale synthesis techniques that maintain the high mobility observed in exfoliated samples. For memory applications, In<sub>2</sub>Se<sub>3</sub> ferroelectric devices represent a promising direction for non-volatile, low-power storage. The most immediate research priority should be improving the endurance of In<sub>2</sub>Se<sub>3</sub> ferroelectric devices beyond their current  $<10^4$  cycle limitation toward the  $>10^{11}$  cycles demonstrated in other van der Waals ferroelectrics. Additionally, the exploration of sliding ferroelectricity in InSe deserves increased attention as a potentially more robust mechanism less susceptible to fatigue and degradation.

Beyond discrete logic or memory functions, the most transformative potential of indium selenides may lie in novel device architectures that leverage their unique combination of properties. For example, FeSFETs utilizing In<sub>2</sub>Se<sub>3</sub> could enable true compute-in-memory functionality, fundamentally changing how information is processed. Similarly, heterojunctions combining different phases of indium selenides could create devices with programmable electronic properties for reconfigurable computing. Material synthesis and process integration challenges remain significant barriers to commercialization. We envision that advances in MOCVD will play a crucial role in overcoming these challenges due to its demonstrated capacity for wafer-scale growth at lower temperatures compatible with BEOL integration. Particularly promising is the development of flow-modulation MOCVD techniques that can reduce nucleation density and promote lateral growth of high-quality films.

On the materials synthesis and discovery side, the largely unexplored In-Ga-Se ternary system represents a particularly exciting frontier for materials discovery and property engineering<sup>158-161</sup>. Alloying InSe with GaSe to form  $\text{In}_{1-x}\text{Ga}_x\text{Se}$  compounds would enable continuous tuning of band structures, effective masses, and optical properties beyond what is possible with phase and thickness control alone. These ternary alloys could offer optimized combinations of mobility, bandgap, and stability tailored for specific applications from high-performance logic to photodetection. Furthermore, the In-Ga-Se system potentially harbors entirely new phases with unique properties at specific compositional ratios, analogous to discoveries in other ternary chalcogenide systems. The development of compositional gradient structures or vertical heterostructures within this material family could yield novel quantum phenomena and device functionalities impossible in binary compounds.

The persistent challenges of oxidation and material stability must be addressed through comprehensive understanding of degradation mechanisms and development of effective passivation strategies. Recent progress in self-limiting oxidation and encapsulation techniques offers promising directions<sup>10,79</sup>, but further work is needed to ensure reliability under real-world operating conditions. As synthesis and integration challenges are progressively solved, their adoption should expand to broader computing applications, potentially enabling new paradigms in energy-efficient information processing that overcome fundamental limitations of current technology.

The transformative potential of indium selenides ultimately depends on continued cross-disciplinary collaboration between materials scientists, device physicists, process engineers, and system architects. By addressing the full spectrum from fundamental properties to practical implementation challenges, this emerging material platform can fulfill its promise as a cornerstone of next-generation, low-power computing technologies.

## Author contributions

D.J., S.S. and N.G. conceived the idea of the content. All authors researched data for this article. S.S. and M.A. contributed substantially to the discussion of the content and wrote the article, with input from W.L. and H.S.S. All authors reviewed and/or edited the content before submission.

## References

- 1 Song, S., Rahaman, M. & Jariwala, D. Can 2D Semiconductors Be Game-Changers for Nanoelectronics and Photonics? *ACS Nano* **18**, 10955-10978, doi:10.1021/acsnano.3c12938 (2024).
- 2 Liu, Y., Huang, Y. & Duan, X. Van der Waals integration before and beyond two-dimensional materials. *Nature* **567**, 323-333, doi:10.1038/s41586-019-1013-x (2019).
- 3 Akinwande, D. *et al.* Graphene and two-dimensional materials for silicon technology. *Nature* **573**, 507-518, doi:10.1038/s41586-019-1573-9 (2019).
- 4 Liu, Y. *et al.* Promises and prospects of two-dimensional transistors. *Nature* **591**, 43-53, doi:10.1038/s41586-021-03339-z (2021).
- 5 Das, S. *et al.* Transistors based on two-dimensional materials for future integrated circuits. *Nature Electronics* **4**, 786-799, doi:10.1038/s41928-021-00670-1 (2021).
- 6 Bandurin, D. A. *et al.* High electron mobility, quantum Hall effect and anomalous optical response in atomically thin InSe. *Nature Nanotechnology* **12**, 223-227, doi:10.1038/nnano.2016.242 (2017).
- 7 Li, M. *et al.* High Mobilities in Layered InSe Transistors with Indium-Encapsulation-Induced Surface Charge Doping. *Advanced Materials* **30**, 1803690, doi:<https://doi.org/10.1002/adma.201803690> (2018).
- 8 Feng, W., Zheng, W., Cao, W. & Hu, P. Back Gated Multilayer InSe Transistors with Enhanced Carrier Mobilities via the Suppression of Carrier Scattering from a Dielectric Interface. *Advanced Materials* **26**, 6587-6593, doi:10.1002/adma.201402427 (2014).
- 9 Gomes da Costa, P., Dandrea, R. G., Wallis, R. F. & Balkanski, M. First-principles study of the electronic structure of  $\gamma$ -InSe and  $\beta$ -InSe. *Phys. Rev. B* **48**, 14135-14141, doi:10.1103/PhysRevB.48.14135 (1993).
- 10 Jiang, J., Xu, L., Qiu, C. & Peng, L.-M. Ballistic two-dimensional InSe transistors. *Nature* **616**, 470-475, doi:10.1038/s41586-023-05819-w (2023).
- 11 Natori, K. Ballistic metal-oxide-semiconductor field effect transistor. *Journal of Applied Physics* **76**, 4879-4890, doi:10.1063/1.357263 (1994).
- 12 Song, S. *et al.* Wafer-scale growth of two-dimensional, phase-pure InSe. *Matter* **6**, 3483-3498, doi:10.1016/j.matt.2023.07.012 (2023).
- 13 Han, W. *et al.* Phase-controllable large-area two-dimensional In<sub>2</sub>Se<sub>3</sub> and ferroelectric

- heterophase junction. *Nature Nanotechnology* **18**, 55-63, doi:10.1038/s41565-022-01257-3 (2023).
- 14 Imai, K., Suzuki, K., Haga, T., Hasegawa, Y. & Abe, Y. Phase diagram of In-Se system and crystal growth of indium monoselenide. *Journal of Crystal Growth* **54**, 501-506, doi:[https://doi.org/10.1016/0022-0248\(81\)90505-4](https://doi.org/10.1016/0022-0248(81)90505-4) (1981).
  - 15 Ding, W. *et al.* Prediction of intrinsic two-dimensional ferroelectrics in In<sub>2</sub>Se<sub>3</sub> and other III<sub>2</sub>-VI<sub>3</sub> van der Waals materials. *Nature Communications* **8**, 14956, doi:10.1038/ncomms14956 (2017).
  - 16 Hu, H. *et al.* Out-of-plane and in-plane ferroelectricity of atom-thick two-dimensional InSe. *Nanotechnology* **32**, 385202, doi:10.1088/1361-6528/ac0ac5 (2021).
  - 17 Sui, F. *et al.* Sliding ferroelectricity in van der Waals layered  $\gamma$ -InSe semiconductor. *Nature Communications* **14**, 36, doi:10.1038/s41467-022-35490-0 (2023).
  - 18 Li, W. *et al.* Emergence of ferroelectricity in a nonferroelectric monolayer. *Nature Communications* **14**, 2757, doi:10.1038/s41467-023-38445-1 (2023).
  - 19 Si, M. *et al.* A ferroelectric semiconductor field-effect transistor. *Nature Electronics* **2**, 580-586, doi:10.1038/s41928-019-0338-7 (2019).
  - 20 Si, M. *et al.* Asymmetric Metal/ $\alpha$ -In<sub>2</sub>Se<sub>3</sub>/Si Crossbar Ferroelectric Semiconductor Junction. *ACS Nano* **15**, 5689-5695, doi:10.1021/acsnano.1c00968 (2021).
  - 21 Miao, J. *et al.* Heterojunction tunnel triodes based on two-dimensional metal selenide and three-dimensional silicon. *Nature Electronics* **5**, 744-751, doi:10.1038/s41928-022-00849-0 (2022).
  - 22 Han, G. *et al.* A new crystal: layer-structured rhombohedral In<sub>3</sub>Se<sub>4</sub>. *CrystEngComm* **16**, 393-398, doi:10.1039/C3CE41815D (2014).
  - 23 Hogg, J. H. C., Sutherland, H. H. & Williams, D. J. The crystal structure of tetraindium triselenide. *Acta Crystallogr B Struct Crystallogr Cryst Chem* **29**, 1590-1593, doi:10.1107/S0567740873005108 (1973).
  - 24 Debbichi, L., Eriksson, O. & Lebègue, S. Two-Dimensional Indium Selenides Compounds: An Ab Initio Study. *The Journal of Physical Chemistry Letters* **6**, 3098-3103, doi:10.1021/acs.jpcclett.5b01356 (2015).
  - 25 Srour, J., Badawi, M., El Haj Hassan, F. & Postnikov, A. Comparative study of structural and electronic properties of GaSe and InSe polytypes. *The Journal of Chemical Physics* **149**, 054106, doi:10.1063/1.5030539 (2018).
  - 26 Pike, N. A. *et al.* Understanding the Origin and Implication of the Indirect-to-Direct Bandgap Transition in Multilayer InSe. *J. Phys. Chem. C* **128**, 7957-7967, doi:10.1021/acs.jpcc.4c01104 (2024).
  - 27 Politano, A. *et al.* Indium selenide: an insight into electronic band structure and surface excitations. *Sci Rep* **7**, 3445, doi:10.1038/s41598-017-03186-x (2017).
  - 28 Hamer, M. J. *et al.* Indirect to Direct Gap Crossover in Two-Dimensional InSe Revealed by Angle-Resolved Photoemission Spectroscopy. *ACS Nano*, acsnano.8b08726, doi:10.1021/acsnano.8b08726 (2019).



- 29 Manjón, F. J. *et al.* Experimental and theoretical study of band structure of InSe and In  $1 - x$  Ga  $x$  Se ( $x < 0.2$ ) under high pressure: Direct to indirect crossovers. *Phys. Rev. B* **63**, 125330, doi:10.1103/PhysRevB.63.125330 (2001).
- 30 Abay, B., Efeoğlu, H. & Yoğurtçu, Y. K. Low-temperature photoluminescence of n-InSe layer semiconductor crystals. *Materials Research Bulletin* **33**, 1401-1410, doi:10.1016/S0025-5408(98)00112-3 (1998).
- 31 Camassel, J., Merle, P., Mathieu, H. & Chevy, A. Excitonic absorption edge of indium selenide. *Phys. Rev. B* **17**, 4718-4725, doi:10.1103/PhysRevB.17.4718 (1978).
- 32 Gürbulak, B. *et al.* Structural characterizations and optical properties of InSe and InSe:Ag semiconductors grown by Bridgman/Stockbarger technique. *Physica E: Low-dimensional Systems and Nanostructures* **64**, 106-111, doi:10.1016/j.physe.2014.07.002 (2014).
- 33 Lei, S. *et al.* Evolution of the Electronic Band Structure and Efficient Photo-Detection in Atomic Layers of InSe. *ACS Nano* **8**, 1263-1272, doi:10.1021/nn405036u (2014).
- 34 Quhe, R. *et al.* Sub-10 nm two-dimensional transistors: Theory and experiment. *Physics Reports* **938**, 1-72, doi:10.1016/j.physrep.2021.07.006 (2021).
- 35 Lundstrom, M. Elementary scattering theory of the Si MOSFET. *IEEE Electron Device Letters* **18**, 361-363, doi:10.1109/55.596937 (1997).
- 36 Julien, C. M. & Balkanski, M. Lithium reactivity with III–VI layered compounds. *Materials Science and Engineering: B* **100**, 263-270, doi:10.1016/S0921-5107(03)00113-2 (2003).
- 37 Dai, M. *et al.* Robust Piezo-Phototronic Effect in Multilayer  $\gamma$ -InSe for High-Performance Self-Powered Flexible Photodetectors. *ACS Nano* **13**, 7291-7299, doi:10.1021/acsnano.9b03278 (2019).
- 38 Borodin, B. R. *et al.* Indirect-to-direct band-gap transition in few-layer  $\beta$ -InSe as probed by photoluminescence spectroscopy. *Phys. Rev. Materials* **8**, 014001, doi:10.1103/PhysRevMaterials.8.014001 (2024).
- 39 Arora, H. & Erbe, A. Recent progress in contact, mobility, and encapsulation engineering of InSe and GaSe. *InfoMat* **3**, 662-693, doi:<https://doi.org/10.1002/inf2.12160> (2021).
- 40 Liu, L. *et al.* Atomically Resolving Polymorphs and Crystal Structures of In<sub>2</sub>Se<sub>3</sub>. *Chemistry of Materials* **31**, 10143-10149, doi:10.1021/acs.chemmater.9b03499 (2019).
- 41 Xue, F. *et al.* Gate-Tunable and Multidirection-Switchable Memristive Phenomena in a Van Der Waals Ferroelectric. *Advanced Materials* **31**, 1901300, doi:<https://doi.org/10.1002/adma.201901300> (2019).
- 42 Wu, Y. *et al.* Stacking selected polarization switching and phase transition in vdW ferroelectric  $\alpha$ -In<sub>2</sub>Se<sub>3</sub> junction devices. *Nature Communications* **15**, 10481, doi:10.1038/s41467-024-54841-7 (2024).
- 43 Xiao, J. *et al.* Intrinsic Two-Dimensional Ferroelectricity with Dipole Locking. *Physical Review Letters* **120**, 227601, doi:10.1103/PhysRevLett.120.227601 (2018).

- 44 Zhang, F. *et al.* Atomic-scale manipulation of polar domain boundaries in monolayer ferroelectric In<sub>2</sub>Se<sub>3</sub>. *Nature Communications* **15**, 718, doi:10.1038/s41467-023-44642-9 (2024).
- 45 Huang, J., Ke, C., Qian, Z. & Liu, S. Competing Charge Transfer and Screening Effects in Two-Dimensional Ferroelectric Capacitors. *Nano Letters* **24**, 6683-6688, doi:10.1021/acs.nanolett.4c01362 (2024).
- 46 Zheng, C. *et al.* Room temperature in-plane ferroelectricity in van der Waals In<sub>2</sub>Se<sub>3</sub>. *Science Advances* **4**, eaar7720, doi:10.1126/sciadv.aar7720 (2018).
- 47 Xu, C. *et al.* Two-dimensional ferroelasticity in van der Waals β'-In<sub>2</sub>Se<sub>3</sub>. *Nature Communications* **12**, 3665, doi:10.1038/s41467-021-23882-7 (2021).
- 48 Wang, L. *et al.* In-Plane Ferrielectric Order in van der Waals β'-In<sub>2</sub>Se<sub>3</sub>. *ACS Nano* **18**, 809-818, doi:10.1021/acsnano.3c09250 (2024).
- 49 Xu, C. *et al.* Two-Dimensional Antiferroelectricity in Nanostripe-Ordered  $\{\mathrm{In}\}_2\{\mathrm{Se}\}_3$ . *Phys. Rev. Lett.* **125**, 047601, doi:10.1103/PhysRevLett.125.047601 (2020).
- 50 Chen, Z. *et al.* Atomic Imaging of Electrically Switchable Striped Domains in β'-In<sub>2</sub>Se<sub>3</sub>. *Advanced Science* **8**, 2100713, doi:10.1002/advs.202100713 (2021).
- 51 Xu, C. *et al.* Two-Dimensional Antiferroelectricity in Nanostripe-Ordered In<sub>2</sub>Se<sub>3</sub>. *Phys. Rev. Lett.* **125**, 047601, doi:10.1103/PhysRevLett.125.047601 (2020).
- 52 Wang, L. *et al.* In-Plane Ferrielectric Order in van der Waals β'-In<sub>2</sub>Se<sub>3</sub>. *ACS Nano* **18**, 809-818, doi:10.1021/acsnano.3c09250 (2024).
- 53 Collins, J. L. *et al.* Electronic Band Structure of In-Plane Ferroelectric van der Waals β'-In<sub>2</sub>Se<sub>3</sub>. *ACS Appl. Electron. Mater.* **2**, 213-219, doi:10.1021/acsaem.9b00699 (2020).
- 54 Zhang, F. *et al.* Atomic-Scale Observation of Reversible Thermally Driven Phase Transformation in 2D In<sub>2</sub>Se<sub>3</sub>. *ACS Nano* **13**, 8004-8011, doi:10.1021/acsnano.9b02764 (2019).
- 55 Balakrishnan, N. *et al.* Quantum confinement and photoresponsivity of β-In<sub>2</sub>Se<sub>3</sub> nanosheets grown by physical vapour transport. *2D Materials* **3**, 025030, doi:10.1088/2053-1583/3/2/025030 (2016).
- 56 Sui, F. *et al.* Atomic-level polarization reversal in sliding ferroelectric semiconductors. *Nature Communications* **15**, 3799, doi:10.1038/s41467-024-48218-z (2024).
- 57 Wang, Y. *et al.* Sliding Ferroelectricity Induced Ultrafast Switchable Photovoltaic Response in ε-InSe Layers. *Advanced Materials* **36**, 2410696, doi:<https://doi.org/10.1002/adma.202410696> (2024).
- 58 Gao, H. *et al.* Picometer-Level In Situ Manipulation of Ferroelectric Polarization in Van der Waals layered InSe. *Advanced Materials* **36**, 2404628, doi:<https://doi.org/10.1002/adma.202404628> (2024).

- 59 Molas, M. R. *et al.* The optical response of monolayer, few-layer and bulk tungsten disulfide. *Nanoscale* **9**, 13128-13141, doi:10.1039/C7NR04672C (2017).
- 60 Li, X. & Zhu, H. Two-dimensional MoS<sub>2</sub>: Properties, preparation, and applications. *Journal of Materiomics* **1**, 33-44, doi:10.1016/j.jmat.2015.03.003 (2015).
- 61 Paylaga, N. T. *et al.* Monolayer indium selenide: an indirect bandgap material exhibits efficient brightening of dark excitons. *npj 2D Mater Appl* **8**, 12, doi:10.1038/s41699-024-00450-3 (2024).
- 62 Borodin, B. R. *et al.* Indirect-to-direct band-gap transition in few-layer  $\beta$ -InSe as probed by photoluminescence spectroscopy. *Phys. Rev. Materials* **8**, 014001, doi:10.1103/PhysRevMaterials.8.014001 (2024).
- 63 Jacobs-Gedrim, R. B. *et al.* Extraordinary Photoresponse in Two-Dimensional In<sub>2</sub>Se<sub>3</sub> Nanosheets. *ACS Nano* **8**, 514-521, doi:10.1021/nn405037s (2014).
- 64 Zhou, J. *et al.* Controlled Synthesis of High-Quality Monolayered  $\alpha$ -In<sub>2</sub>Se<sub>3</sub> via Physical Vapor Deposition. *Nano Letters* **15**, 6400-6405, doi:10.1021/acs.nanolett.5b01590 (2015).
- 65 Balakrishnan, N. *et al.* Quantum confinement and photoresponsivity of  $\beta$ -In<sub>2</sub>Se<sub>3</sub> nanosheets grown by physical vapour transport. *2D Materials* **3**, 025030, doi:10.1088/2053-1583/3/2/025030 (2016).
- 66 Quereda, J. *et al.* Strong Quantum Confinement Effect in the Optical Properties of Ultrathin  $\alpha$ -In<sub>2</sub>Se<sub>3</sub>. *Advanced Optical Materials* **4**, 1939-1943, doi:10.1002/adom.201600365 (2016).
- 67 Wu, H. *et al.* Anomalous interlayer vibrations in few-layer InSe induced by weak intralayer bonding. *Applied Physics Letters* **123**, 053103, doi:10.1063/5.0166258 (2023).
- 68 Wan, S. *et al.* Nonvolatile Ferroelectric Memory Effect in Ultrathin  $\alpha$ -In<sub>2</sub>Se<sub>3</sub>. *Advanced Functional Materials* **29**, 1808606, doi:<https://doi.org/10.1002/adfm.201808606> (2019).
- 69 Parker, J. & Gu, Y. Highly Efficient Polarization-Controlled Electrical Conductance Modulation in a van der Waals Ferroelectric/Semiconductor Heterostructure. *Advanced Electronic Materials* **8**, 2200413, doi:<https://doi.org/10.1002/aelm.202200413> (2022).
- 70 Yang, T. H. *et al.* Ferroelectric transistors based on shear-transformation-mediated rhombohedral-stacked molybdenum disulfide. *Nature Electronics*, doi:10.1038/s41928-023-01073-0 (2023).
- 71 Niu, R. *et al.* Giant ferroelectric polarization in a bilayer graphene heterostructure. *Nature Communications* **13**, 6241, doi:10.1038/s41467-022-34104-z (2022).
- 72 Zheng, Z. *et al.* Unconventional ferroelectricity in moiré heterostructures. *Nature* **588**, 71-76, doi:10.1038/s41586-020-2970-9 (2020).
- 73 Wang, X. *et al.* Van der Waals engineering of ferroelectric heterostructures for long-retention memory. *Nature Communications* **12**, 1109, doi:10.1038/s41467-021-21320-2 (2021).

- 74 Kwon, K. C. *et al.* In-Plane Ferroelectric Tin Monosulfide and Its Application in a Ferroelectric Analog Synaptic Device. *ACS Nano* **14**, 7628-7638, doi:10.1021/acsnano.0c03869 (2020).
- 75 Gao, P. *et al.* Possible absence of critical thickness and size effect in ultrathin perovskite ferroelectric films. *Nature Communications* **8**, 15549, doi:10.1038/ncomms15549 (2017).
- 76 Cheema, S. S. *et al.* Enhanced ferroelectricity in ultrathin films grown directly on silicon. *Nature* **580**, 478-482, doi:10.1038/s41586-020-2208-x (2020).
- 77 Kim, K.-H., Karpov, I., Olsson, R. H. & Jariwala, D. Wurtzite and fluorite ferroelectric materials for electronic memory. *Nature Nanotechnology* **18**, 422-441, doi:10.1038/s41565-023-01361-y (2023).
- 78 Gong, N. & Ma, T. P. Why Is FE–HfO<sub>2</sub> More Suitable Than PZT or SBT for Scaled Nonvolatile 1-T Memory Cell? A Retention Perspective. *IEEE Electron Device Letters* **37**, 1123-1126, doi:10.1109/LED.2016.2593627 (2016).
- 79 Ho, P.-H. *et al.* High-Mobility InSe Transistors: The Role of Surface Oxides. *ACS Nano* **11**, 7362-7370, doi:10.1021/acsnano.7b03531 (2017).
- 80 Mudd, G. W. *et al.* Tuning the Bandgap of Exfoliated InSe Nanosheets by Quantum Confinement. *Advanced Materials* **25**, 5714-5718, doi:<https://doi.org/10.1002/adma.201302616> (2013).
- 81 Li, C. *et al.* Room-temperature Near-infrared Excitonic Lasing from Mechanically Exfoliated InSe Microflake. *ACS Nano* **16**, 1477-1485, doi:10.1021/acsnano.1c09844 (2022).
- 82 Li, Z. *et al.* High-Performance Photo-Electrochemical Photodetector Based on Liquid-Exfoliated Few-Layered InSe Nanosheets with Enhanced Stability. *Advanced Functional Materials* **28**, 1705237, doi:<https://doi.org/10.1002/adfm.201705237> (2018).
- 83 Kang, J. *et al.* Solution-Based Processing of Optoelectronically Active Indium Selenide. *Advanced Materials* **30**, 1802990, doi:<https://doi.org/10.1002/adma.201802990> (2018).
- 84 He, J. *et al.* Solution-processed wafer-scale indium selenide semiconductor thin films with high mobilities. *Nature Electronics*, doi:10.1038/s41928-025-01338-w (2025).
- 85 Shi, H. *et al.* Ultrafast Electrochemical Synthesis of Defect-Free In<sub>2</sub>Se<sub>3</sub> Flakes for Large-Area Optoelectronics. *Advanced Materials* **32**, 1907244, doi:<https://doi.org/10.1002/adma.201907244> (2020).
- 86 Tang, A. *et al.* Toward Low-Temperature Solid-Source Synthesis of Monolayer MoS<sub>2</sub>. *ACS Appl Mater Interfaces* **13**, 41866-41874, doi:10.1021/acscami.1c06812 (2021).
- 87 Poh, S. M. *et al.* Molecular-Beam Epitaxy of Two-Dimensional In<sub>2</sub>Se<sub>3</sub> and Its Giant Electroresistance Switching in Ferroresistive Memory Junction. *Nano Letters* **18**, 6340-6346, doi:10.1021/acs.nanolett.8b02688 (2018).
- 88 Claro, M. S., Grzonka, J., Nicoara, N., Ferreira, P. J. & Sadewasser, S. Wafer-Scale Fabrication of 2D  $\beta$ -In<sub>2</sub>Se<sub>3</sub> Photodetectors. *Advanced Optical Materials* **9**, doi:10.1002/adom.202001034 (2020).

- 89 Poh, S. M. *et al.* Molecular-Beam Epitaxy of Two-Dimensional In<sub>2</sub>Se<sub>3</sub> and Its Giant Electroresistance Switching in Ferroresistive Memory Junction. *Nano Lett* **18**, 6340-6346, doi:10.1021/acs.nanolett.8b02688 (2018).
- 90 Si, K. *et al.* Quasi-equilibrium growth of inch-scale single-crystal monolayer  $\alpha$ -In<sub>2</sub>Se<sub>3</sub> on fluor-phlogopite. *Nature Communications* **15**, 7471, doi:10.1038/s41467-024-51322-9 (2024).
- 91 Rashid, R. *et al.* Shape-control growth of 2D-In<sub>2</sub>Se<sub>3</sub> with out-of-plane ferroelectricity by chemical vapor deposition. *Nanoscale* **12**, 20189-20201, doi:10.1039/C9NR10207H (2020).
- 92 Zhou, J. *et al.* Controlled Synthesis of High-Quality Monolayered  $\alpha$ -In<sub>2</sub>Se<sub>3</sub> via Physical Vapor Deposition. *Nano Letters* **15**, 6400-6405, doi:10.1021/acs.nanolett.5b01590 (2015).
- 93 Huang, W., Gan, L., Li, H., Ma, Y. & Zhai, T. Phase-Engineered Growth of Ultrathin InSe Flakes by Chemical Vapor Deposition for High-Efficiency Second Harmonic Generation. *Chemistry – A European Journal* **24**, 15678-15684, doi:<https://doi.org/10.1002/chem.201803634> (2018).
- 94 Chang, H.-C. *et al.* Synthesis of Large-Area InSe Monolayers by Chemical Vapor Deposition. *Small* **14**, 1802351, doi:<https://doi.org/10.1002/sml.201802351> (2018).
- 95 Zhang, X. *et al.* Epitaxial growth of few-layer  $\beta$ -In<sub>2</sub>Se<sub>3</sub> thin films by metalorganic chemical vapor deposition. *Journal of Crystal Growth* **533**, 125471, doi:<https://doi.org/10.1016/j.jcrysgro.2019.125471> (2020).
- 96 Hu, Y. X. *et al.* Temperature-dependent growth of few layer  $\beta$ -InSe and  $\alpha$ -InSe single crystals for optoelectronic device. *Semiconductor Science and Technology* **33**, doi:10.1088/1361-6641/aae629 (2018).
- 97 Liu, C. *et al.* Understanding epitaxial growth of two-dimensional materials and their homostructures. *Nature Nanotechnology* **19**, 907-918, doi:10.1038/s41565-024-01704-3 (2024).
- 98 Chang, Y.-R. *et al.* Surface Oxidation Doping to Enhance Photogenerated Carrier Separation Efficiency for Ultrahigh Gain Indium Selenide Photodetector. *ACS Photonics* **4**, 2930-2936, doi:10.1021/acsp Photonics.7b01030 (2017).
- 99 Balakrishnan, N. *et al.* Engineering p–n junctions and bandgap tuning of InSe nanolayers by controlled oxidation. *2D Materials* **4**, 025043, doi:10.1088/2053-1583/aa61e0 (2017).
- 100 Shi, L. *et al.* Oxidation Mechanism and Protection Strategy of Ultrathin Indium Selenide: Insight from Theory. *The Journal of Physical Chemistry Letters* **8**, 4368-4373, doi:10.1021/acs.jpcl.7b02059 (2017).
- 101 Yan, S. *et al.* Phase Instability in van der Waals In<sub>2</sub>Se<sub>3</sub> Determined by Surface Coordination. *Angewandte Chemie International Edition* **62**, e202300302, doi:<https://doi.org/10.1002/anie.202300302> (2023).
- 102 Chang, H. C. *et al.* Synthesis of Large-Area InSe Monolayers by Chemical Vapor Deposition. *Small* **14**, e1802351, doi:10.1002/sml.201802351 (2018).

- 103 Si, K. *et al.* Quasi-equilibrium growth of inch-scale single-crystal monolayer alpha-In(2)Se(3) on fluor-phlogopite. *Nat Commun* **15**, 7471, doi:10.1038/s41467-024-51322-9 (2024).
- 104 Yang, K. *et al.* Controllable growth  $\alpha$ -In<sub>2</sub>Se<sub>3</sub> flakes by chemical vapor deposition. *Results in Physics* **51**, doi:10.1016/j.rinp.2023.106643 (2023).
- 105 Li, X. *et al.* Two-dimensional GaSe/MoSe<sub>2</sub> misfit bilayer heterojunctions by van der Waals epitaxy. *Sci Adv* **2**, e1501882, doi:10.1126/sciadv.1501882 (2016).
- 106 Li, X. *et al.* Controlled vapor phase growth of single crystalline, two-dimensional GaSe crystals with high photoresponse. *Sci Rep* **4**, 5497, doi:10.1038/srep05497 (2014).
- 107 Xue, W. *et al.* Discovery of Robust Ferroelectricity in 2D Defective Semiconductor alpha-Ga(2) Se(3). *Small* **18**, e2105599, doi:10.1002/sml.202105599 (2022).
- 108 Zhou, N. *et al.* Precise Synthesis and Broadband Photoresponse of Two-Dimensional Intrinsic Vacancy Semiconductor. *Small Structures* **5**, doi:10.1002/sstr.202400062 (2024).
- 109 Cao, W. *et al.* The future transistors. *Nature* **620**, 501-515, doi:10.1038/s41586-023-06145-x (2023).
- 110 Pal, A., Chavan, T., Jabbour, J., Cao, W. & Banerjee, K. Three-dimensional transistors with two-dimensional semiconductors for future CMOS scaling. *Nature Electronics* **7**, 1147-1157, doi:10.1038/s41928-024-01289-8 (2024).
- 111 Bergeron, H. *et al.* Large-area optoelectronic-grade InSe thin films via controlled phase evolution. *Applied Physics Reviews* **7**, 041402, doi:10.1063/5.0023080 (2020).
- 112 Zhao, Q. *et al.* The role of traps in the photocurrent generation mechanism in thin InSe photodetectors. *Mater. Horiz.* **7**, 252-262, doi:10.1039/C9MH01020C (2020).
- 113 Wang, Y. *et al.* Molecular Doping of 2D Indium Selenide for Ultrahigh Performance and Low-Power Consumption Broadband Photodetectors. *Advanced Functional Materials* **31**, 2103353, doi:10.1002/adfm.202103353 (2021).
- 114 Jiang, J. *et al.* Stable InSe transistors with high-field effect mobility for reliable nerve signal sensing. *npj 2D Mater Appl* **3**, 29, doi:10.1038/s41699-019-0110-x (2019).
- 115 Zhang, S. *et al.* The role of hybrid dielectric interfaces in improving the performance of multilayer InSe transistors. *J. Mater. Chem. C* **8**, 6701-6709, doi:10.1039/D0TC00331J (2020).
- 116 Chen, Y.-H. *et al.* Oxidized-monolayer tunneling barrier for strong Fermi-level depinning in layered InSe transistors. *npj 2D Mater Appl* **3**, 49, doi:10.1038/s41699-019-0133-3 (2019).
- 117 Tsai, T.-H. *et al.* High-Mobility InSe Transistors: The Nature of Charge Transport. *ACS Applied Materials & Interfaces* **11**, 35969-35976, doi:10.1021/acsami.9b11052 (2019).
- 118 Li, M. *et al.* High Mobilities in Layered InSe Transistors with Indium-Encapsulation-Induced Surface Charge Doping. *Advanced Materials* **30**, 1803690, doi:10.1002/adma.201803690 (2018).
- 119 Zeng, J. *et al.* Gate-tunable weak antilocalization in a few-layer InSe. *Phys. Rev. B* **98**,

- 125414, doi:10.1103/PhysRevB.98.125414 (2018).
- 120 Arora, H. *et al.* Effective Hexagonal Boron Nitride Passivation of Few-Layered InSe and GaSe to Enhance Their Electronic and Optical Properties. *ACS Applied Materials & Interfaces* **11**, 43480-43487, doi:10.1021/acsami.9b13442 (2019).
- 121 Li, Z. *et al.* Enhancement of Carrier Mobility in Multilayer InSe Transistors by van der Waals Integration. *Nanomaterials* **14**, 382, doi:10.3390/nano14040382 (2024).
- 122 Jiang, J., Xu, L., Qiu, C. & Peng, L. M. Ballistic two-dimensional InSe transistors. *Nature* **616**, 470-475, doi:10.1038/s41586-023-05819-w (2023).
- 123 Pasquale, G. *et al.* Electrical detection of the flat-band dispersion in van der Waals field-effect structures. *Nature Nanotechnology* **18**, 1416-1422, doi:10.1038/s41565-023-01489-x (2023).
- 124 Gao, A. *et al.* Observation of ballistic avalanche phenomena in nanoscale vertical InSe/BP heterostructures. *Nature Nanotechnology* **14**, 217-222, doi:10.1038/s41565-018-0348-z (2019).
- 125 Pang, C.-S., Wu, P., Appenzeller, J. & Chen, Z. in *2020 IEEE International Electron Devices Meeting (IEDM)* 3.4.1-3.4.4 (2020).
- 126 Li, W. *et al.* Approaching the quantum limit in two-dimensional semiconductor contacts. *Nature* **613**, 274-279, doi:10.1038/s41586-022-05431-4 (2023).
- 127 Leblanc, C., Song, S. & Jariwala, D. 2D Ferroelectrics and ferroelectrics with 2D: Materials and device prospects. *Current Opinion in Solid State and Materials Science* **32**, 101178, doi:<https://doi.org/10.1016/j.cossms.2024.101178> (2024).
- 128 Wang, X. *et al.* Interfacial ferroelectricity in rhombohedral-stacked bilayer transition metal dichalcogenides. *Nature Nanotechnology* **17**, 367-371, doi:10.1038/s41565-021-01059-z (2022).
- 129 Luo, Y. *et al.* Robust Giant Tunnel Electroresistance and Negative Differential Resistance in 2D Semiconductor/ $\alpha$ -In<sub>2</sub>Se<sub>3</sub> Ferroelectric Tunnel Junctions. *Advanced Functional Materials* **34**, doi:10.1002/adfm.202407253 (2024).
- 130 Si, M. *et al.* Asymmetric Metal/ $\alpha$ -In<sub>2</sub>Se<sub>3</sub>/Si Crossbar Ferroelectric Semiconductor Junction. *ACS Nano* **15**, 5689-5695, doi:10.1021/acsnano.1c00968 (2021).
- 131 Tang, W. *et al.* A van der Waals Ferroelectric Tunnel Junction for Ultrahigh-Temperature Operation Memory. *Small Methods* **6**, 2101583, doi:<https://doi.org/10.1002/smt.202101583> (2022).
- 132 Luo, Y. *et al.* Robust Giant Tunnel Electroresistance and Negative Differential Resistance in 2D Semiconductor/ $\alpha$ -In<sub>2</sub>Se<sub>3</sub> Ferroelectric Tunnel Junctions. *Advanced Functional Materials* **34**, 2407253, doi:<https://doi.org/10.1002/adfm.202407253> (2024).
- 133 Wang, S. *et al.* Two-dimensional ferroelectric channel transistors integrating ultra-fast memory and neural computing. *Nat Commun* **12**, 53, doi:10.1038/s41467-020-20257-2 (2021).

- 134 Miao, S., Nitta, R., Izawa, S. & Majima, Y. Bottom Contact 100 nm Channel-Length  $\alpha$ -In<sub>2</sub>Se<sub>3</sub> In-Plane Ferroelectric Memory. *Adv Sci (Weinh)* **10**, e2303032, doi:10.1002/advs.202303032 (2023).
- 135 Han, W. *et al.* Phase-controllable large-area two-dimensional In<sub>2</sub>Se<sub>3</sub> and ferroelectric heterophase junction. *Nat Nanotechnol* **18**, 55-63, doi:10.1038/s41565-022-01257-3 (2023).
- 136 Xue, F. *et al.* Giant Ferroelectric Resistance Switching Controlled by a Modulatory Terminal for Low-Power Neuromorphic In-Memory Computing. *Adv Mater* **33**, e2008709, doi:10.1002/adma.202008709 (2021).
- 137 Li, Y. *et al.* Nonvolatile Memory Device Based on the Ferroelectric Metal/Ferroelectric Semiconductor Junction. *Nano Letters*, doi:10.1021/acs.nanolett.4c05887 (2025).
- 138 Li, J. *et al.* Giant Electroresistance in Ferroionic Tunnel Junctions. *iScience* **16**, 368-377, doi:<https://doi.org/10.1016/j.isci.2019.05.043> (2019).
- 139 Wang, Q. *et al.* Extraordinary tunnel electroresistance in layer-by-layer engineered van der Waals ferroelectric tunnel junctions. *Matter* **5**, 4425-4436, doi:10.1016/j.matt.2022.10.014 (2022).
- 140 Khan, A. I., Keshavarzi, A. & Datta, S. The future of ferroelectric field-effect transistor technology. *Nature Electronics* **3**, 588-597, doi:10.1038/s41928-020-00492-7 (2020).
- 141 Luo, Q. *et al.* A highly CMOS compatible hafnia-based ferroelectric diode. *Nature Communications* **11**, 1391, doi:10.1038/s41467-020-15159-2 (2020).
- 142 Florent, K. *et al.* in *2018 IEEE International Electron Devices Meeting (IEDM)*. 2.5.1-2.5.4.
- 143 Song, S. *et al.* High Current and Carrier Densities in 2D MoS<sub>2</sub>/AlScN Field-Effect Transistors via Ferroelectric Gating and Ohmic Contacts. *ACS Nano*, doi:10.1021/acsnano.4c17301 (2025).
- 144 Ma, T. P. & Jin-Ping, H. Why is nonvolatile ferroelectric memory field-effect transistor still elusive? *IEEE Electron Device Letters* **23**, 386-388, doi:10.1109/LED.2002.1015207 (2002).
- 145 Liu, F. *et al.* Room-temperature ferroelectricity in CuInP<sub>2</sub>S<sub>6</sub> ultrathin flakes. *Nature Communications* **7**, 12357, doi:10.1038/ncomms12357 (2016).
- 146 Higashitarumizu, N. *et al.* Purely in-plane ferroelectricity in monolayer SnS at room temperature. *Nature Communications* **11**, 2428, doi:10.1038/s41467-020-16291-9 (2020).
- 147 Wang, S. *et al.* Two-dimensional ferroelectric channel transistors integrating ultra-fast memory and neural computing. *Nature Communications* **12**, 53, doi:10.1038/s41467-020-20257-2 (2021).
- 148 Feng, Z. *et al.* Tribo-ferro-optoelectronic neuromorphic transistor of  $\alpha$ -In<sub>2</sub>Se<sub>3</sub>. *Brain-X* **1**, e24, doi:<https://doi.org/10.1002/brx2.24> (2023).
- 149 Duong, N. T. *et al.* Coupled Ferroelectric-Photonic Memory in a Retinomorph Hardware for In-Sensor Computing. *Advanced Science* **11**, 2303447,



- doi:<https://doi.org/10.1002/advs.202303447> (2024).
- 150 Chen, Y. *et al.* Highly Linear and Symmetric Synaptic Memtransistors Based on Polarization Switching in Two-Dimensional Ferroelectric Semiconductors. *Small* **18**, 2203611, doi:<https://doi.org/10.1002/smll.202203611> (2022).
- 151 Yasuda, K. *et al.* Ultrafast high-endurance memory based on sliding ferroelectrics. *Science* **385**, 53-56, doi:doi:10.1126/science.adp3575 (2024).
- 152 Yurchuk, E. *et al.* in *2014 IEEE International Reliability Physics Symposium*. 2E.5.1-2E.5.5.
- 153 Park, S., Lee, D., Kang, J., Choi, H. & Park, J. H. Laterally gated ferroelectric field effect transistor (LG-FeFET) using alpha-In(2)Se(3) for stacked in-memory computing array. *Nat Commun* **14**, 6778, doi:10.1038/s41467-023-41991-3 (2023).
- 154 Kim, K. H. *et al.* Scalable CMOS back-end-of-line-compatible AlScN/two-dimensional channel ferroelectric field-effect transistors. *Nat Nanotechnol* **18**, 1044-1050, doi:10.1038/s41565-023-01399-y (2023).
- 155 Wu, J. *et al.* High tunnelling electroresistance in a ferroelectric van der Waals heterojunction via giant barrier height modulation. *Nature Electronics* **3**, 466-472, doi:10.1038/s41928-020-0441-9 (2020).
- 156 Yang, T. H. *et al.* Ferroelectric transistors based on shear-transformation-mediated rhombohedral-stacked molybdenum disulfide. *Nature Electronics* **7**, 29-38, doi:10.1038/s41928-023-01073-0 (2023).
- 157 Lim, T. *et al.* Large-Area Growth of Ferroelectric 2D gamma-In(2) Se(3) Semiconductor by Spray Pyrolysis for Next-Generation Memory. *Adv Mater* **36**, e2308301, doi:10.1002/adma.202308301 (2024).
- 158 Gousskov, A., Camassel, J. & Gousskov, L. Growth and characterization of III–VI layered crystals like GaSe, GaTe, InSe, GaSe<sub>1-x</sub>Te<sub>x</sub> and GaIn<sub>1-x</sub>Se. *Progress in Crystal Growth and Characterization* **5**, 323-413, doi:[https://doi.org/10.1016/0146-3535\(82\)90004-1](https://doi.org/10.1016/0146-3535(82)90004-1) (1982).
- 159 Yu, M. *et al.* Synthesis of Two-Dimensional Alloy Ga<sub>0.84</sub>In<sub>0.16</sub>Se Nanosheets for High-Performance Photodetector. *ACS Applied Materials & Interfaces* **10**, 43299-43304, doi:10.1021/acsami.8b15317 (2018).
- 160 Tran, Q. T. *et al.* Molecular Beam Epitaxy of Mixed Dimensional InGaSe/GaSe Hybrid Heterostructures on C-Sapphire. *ACS Appl. Electron. Mater.* **6**, 7448-7455, doi:10.1021/acsaelm.4c01325 (2024).
- 161 Amiraslanov, I. R. *et al.* Synthesis and characterization of new indium gallium selenides of the InSe-GaSe system. *Journal of Solid State Chemistry* **304**, 122569, doi:<https://doi.org/10.1016/j.jssc.2021.122569> (2021).

**Table S1. Comparisons of ferroelectricity of vdW indium selenides with other 2D ferroelectric materials/systems.** The label "Bernal BLG" refers to Bernal-stacked bilayer graphene sandwiched with hBN layers. "R-stacked" refers to rhombohedral-stacked crystals, which are either naturally grown or CVD-grown ones.

Material	OOP/IP direction	Remnant or internal polarization	Coercive field or energy barrier	Curie temp.	Prep. methods
<b><math>\alpha</math>-phase <math>\text{In}_2\text{Se}_3</math></b>	OOP and IP (Ref. <sup>1</sup> )	0.92 $\mu\text{C}/\text{cm}^2$ (OOP; Ref. <sup>2</sup> ) 0.97 (OOP) and 8.0 $\mu\text{C}/\text{cm}^2$ (IP)(DFT; Ref. <sup>3</sup> )	0.33 V/nm (OOP; Ref. <sup>4</sup> ) 300 kV/cm (OOP;Ref. <sup>5</sup> )	700 K (Ref. <sup>6</sup> )	CVD (Ref. <sup>4,6,7</sup> ) ME (Ref. <sup>5,7,8</sup> )
<b><math>\beta'</math>-phase <math>\text{In}_2\text{Se}_3</math></b>	IP (Ref. <sup>9</sup> )	0.199 $\mu\text{C}/\text{cm}^2$ (DFT; Ref. <sup>9</sup> )	0.27 eV/unit cell (DFT; Ref. <sup>9</sup> )	477 K (Ref. <sup>9</sup> )	ME (Ref. <sup>9</sup> ) CVD (Ref. <sup>10</sup> ) MBE (Ref. <sup>11</sup> )
<b><math>\gamma</math>-phase <math>\text{InSe}</math></b>	OOP (Ref. <sup>12,13</sup> )	1.0 pC/m (DFT; Ref. <sup>13</sup> )	0.014 eV/unit cell (DFT; Ref. <sup>13</sup> )	Above RT (Ref. <sup>12,13</sup> )	ME (Ref. <sup>12,13</sup> )
<b><math>\epsilon</math>-phase <math>\text{InSe}</math></b>	OOP (Ref. <sup>14</sup> )	0.04 pC/m (DFT; Ref. <sup>14</sup> )	0.022 eV/unit cell (DFT; Ref. <sup>14</sup> )	Above RT (Ref. <sup>14</sup> )	ME (Ref. <sup>14</sup> )
<b><math>\text{CuInP}_2\text{S}_6</math></b>	OOP (Ref. <sup>15,16</sup> )	4 $\mu\text{C}/\text{cm}^2$ (200 nm; Ref. <sup>16</sup> )	300 kV/cm (Ref. <sup>16</sup> )	320 K (Ref. <sup>15</sup> )	ME (Ref. <sup>16</sup> )
<b><math>\alpha</math>-phase <math>\text{SnS}</math></b>	IP (Ref. <sup>17</sup> )	3 $\mu\text{C}/\text{m}$ (Ref. <sup>17</sup> ) 17.5 $\mu\text{C}/\text{cm}^2$ (Ref. <sup>18</sup> ) 2.62 $\times 10^{-10}$ C/m (DFT; Ref. <sup>19</sup> )	25 kV/cm (Ref. <sup>17</sup> ) 20 kV/cm (Ref. <sup>18</sup> ) 10.7 kV/cm (Ref. <sup>20</sup> )	Above RT (Ref. <sup>17,18</sup> ) 1200 K (DFT; Ref. <sup>19</sup> )	CVD (Ref. <sup>17,18</sup> ) MBE (Ref. <sup>20</sup> )
<b><math>\alpha</math>-phase <math>\text{SnSe}</math></b>	IP (Ref. <sup>21</sup> )	1.5 $\times 10^{-10}$ C/m (DFT; Ref. <sup>21</sup> ) 1.51 $\times 10^{-10}$ C/m (DFT; Ref. <sup>19</sup> )	-	380-400 K (Ref. <sup>21</sup> ) 326 K (DFT; Ref. <sup>19</sup> )	MBE (Ref. <sup>21</sup> )
<b><math>\alpha</math>-phase <math>\text{SnTe}</math></b>	IP (Ref. <sup>22</sup> )	13-22 $\mu\text{C}/\text{cm}^2$ (DFT; Ref. <sup>22</sup> )	-	Above RT for bilayer; 270 K for monolayer (Ref. <sup>22</sup> )	MBE (Ref. <sup>22</sup> )
<b><math>\alpha</math>-phase <math>\text{GeS}</math></b>	IP (Ref. <sup>23</sup> )	5.06 $\times 10^{-10}$ C/m (DFT; Ref. <sup>19</sup> )	18.1 kV/cm (Ref. <sup>23</sup> )	6400 K (DFT; Ref. <sup>19</sup> )	ME (Ref. <sup>23</sup> )
<b><math>\alpha</math>-phase <math>\text{GeSe}</math></b>	IP (Ref. <sup>24</sup> )	3.67 $\times 10^{-10}$ C/m (DFT; Ref. <sup>19</sup> )	-	700 K (Ref. <sup>24</sup> ) 2300 K (DFT; Ref. <sup>19</sup> )	ME (Ref. <sup>24</sup> )
<b><math>\alpha</math>-phase <math>\text{Bi}</math></b>	IP (Ref. <sup>25</sup> )	0.41 $\times 10^{-10}$ C/m (DFT; Ref. <sup>25</sup> )	15.7 mV/Å (DFT; Ref. <sup>25</sup> )	210 K (Ref. <sup>25</sup> )	MBE (Ref. <sup>25</sup> )

<b>T<sub>d</sub>-phase WTe<sub>2</sub></b>	OOP (Ref. <sup>26,27</sup> )	0.19 $\mu\text{C}/\text{cm}^2$ (Ref. <sup>26</sup> ) $10^4$ e/cm (Ref. <sup>27</sup> )	0.70 eV/f.u. (Ref. <sup>26</sup> )	350 K (Ref. <sup>27</sup> )	ME (Ref. <sup>26</sup> )
<b>Bernal- stacked BLG/BN</b>	OOP (Ref. <sup>28-30</sup> )	0.9-5.0 pC/m (Ref. <sup>28</sup> ) 0.05-0.18 $\mu\text{C}/\text{cm}^2$ (Ref. <sup>29</sup> )	0.2-0.4 V/nm (Ref. <sup>28,29</sup> )	200 K (Ref. <sup>29</sup> ), above RT (Ref. <sup>30</sup> )	ME (Ref. <sup>28- 30</sup> )
<b>R-stacked MoS<sub>2</sub></b>	OOP (Ref. <sup>31</sup> )	0.4 $\mu\text{C}/\text{cm}^2$ (Ref. <sup>31</sup> ) 0.53 pC/m (Ref. <sup>32</sup> )	0.036 V/nm (Ref. <sup>31</sup> )	Above RT (Ref. <sup>31,32</sup> )	ME (Ref. <sup>32</sup> ) CVD (Ref. <sup>31</sup> )
<b>R-stacked WSe<sub>2</sub></b>	OOP (Ref. <sup>33</sup> )	1.97 pC/m (Ref. <sup>33</sup> )	0.3 V/nm (Ref. <sup>33</sup> )	Above RT (Ref. <sup>33</sup> )	ME (Ref. <sup>33</sup> ) CVD (Ref. <sup>34</sup> )

## Supplementary References

- 1 Xue, F. *et al.* Gate-Tunable and Multidirection-Switchable Memristive Phenomena in a Van Der Waals Ferroelectric. *Advanced Materials* **31**, 1901300, doi:<https://doi.org/10.1002/adma.201901300> (2019).
- 2 Wan, S. *et al.* Nonvolatile Ferroelectric Memory Effect in Ultrathin  $\alpha$ -In<sub>2</sub>Se<sub>3</sub>. *Advanced Functional Materials* **29**, 1808606, doi:<https://doi.org/10.1002/adfm.201808606> (2019).
- 3 Jiang, X., Feng, Y., Chen, K.-Q. & Tang, L.-M. The coexistence of ferroelectricity and topological phase transition in monolayer  $\alpha$ -In<sub>2</sub>Se<sub>3</sub> under strain engineering. *Journal of Physics: Condensed Matter* **32**, 105501, doi:10.1088/1361-648X/ab58f1 (2020).
- 4 Io, W. F. *et al.* Temperature- and thickness-dependence of robust out-of-plane ferroelectricity in CVD grown ultrathin van der Waals  $\alpha$ -In<sub>2</sub>Se<sub>3</sub> layers. *Nano Res.* **13**, 1897-1902, doi:10.1007/s12274-020-2640-0 (2020).
- 5 Parker, J. & Gu, Y. Highly Efficient Polarization-Controlled Electrical Conductance Modulation in a van der Waals Ferroelectric/Semiconductor Heterostructure. *Advanced Electronic Materials* **8**, 2200413, doi:<https://doi.org/10.1002/aelm.202200413> (2022).
- 6 Xiao, J. *et al.* Intrinsic Two-Dimensional Ferroelectricity with Dipole Locking. *Physical Review Letters* **120**, 227601, doi:10.1103/PhysRevLett.120.227601 (2018).
- 7 Zhou, Y. *et al.* Out-of-Plane Piezoelectricity and Ferroelectricity in Layered  $\alpha$ -In<sub>2</sub>Se<sub>3</sub> Nanoflakes. *Nano Letters* **17**, 5508-5513, doi:10.1021/acs.nanolett.7b02198 (2017).
- 8 Xue, F. *et al.* Room-Temperature Ferroelectricity in Hexagonally Layered  $\alpha$ -In<sub>2</sub>Se<sub>3</sub> Nanoflakes down to the Monolayer Limit. *Advanced Functional Materials* **28**, 1803738, doi:<https://doi.org/10.1002/adfm.201803738> (2018).
- 9 Zheng, C. *et al.* Room temperature in-plane ferroelectricity in van der Waals In<sub>2</sub>Se<sub>3</sub>. *Science Advances* **4**, eaar7720, doi:10.1126/sciadv.aar7720 (2018).
- 10 Xu, C. *et al.* Two-dimensional ferroelasticity in van der Waals  $\beta'$ -In<sub>2</sub>Se<sub>3</sub>. *Nature Communications* **12**, 3665, doi:10.1038/s41467-021-23882-7 (2021).
- 11 Zhang, Z. *et al.* Atomic Visualization and Switching of Ferroelectric Order in  $\beta$ -In<sub>2</sub>Se<sub>3</sub> Films at the Single Layer Limit. *Advanced Materials* **34**, 2106951, doi:<https://doi.org/10.1002/adma.202106951> (2022).
- 12 Sui, F. *et al.* Sliding ferroelectricity in van der Waals layered  $\gamma$ -InSe semiconductor. *Nature Communications* **14**, 36, doi:10.1038/s41467-022-35490-0 (2023).
- 13 Gao, H. *et al.* Picometer-Level In Situ Manipulation of Ferroelectric Polarization in Van der Waals layered InSe. *Advanced Materials* **36**, 2404628, doi:<https://doi.org/10.1002/adma.202404628> (2024).
- 14 Wang, Y. *et al.* Sliding Ferroelectricity Induced Ultrafast Switchable Photovoltaic Response in  $\epsilon$ -InSe Layers. *Advanced Materials* **36**, 2410696, doi:<https://doi.org/10.1002/adma.202410696> (2024).
- 15 Liu, F. *et al.* Room-temperature ferroelectricity in CuInP<sub>2</sub>S<sub>6</sub> ultrathin flakes. *Nature*

- Communications* **7**, 12357, doi:10.1038/ncomms12357 (2016).
- 16 Wang, X. *et al.* Van der Waals engineering of ferroelectric heterostructures for long-retention memory. *Nature Communications* **12**, 1109, doi:10.1038/s41467-021-21320-2 (2021).
  - 17 Higashitarumizu, N. *et al.* Purely in-plane ferroelectricity in monolayer SnS at room temperature. *Nature Communications* **11**, 2428, doi:10.1038/s41467-020-16291-9 (2020).
  - 18 Kwon, K. C. *et al.* In-Plane Ferroelectric Tin Monosulfide and Its Application in a Ferroelectric Analog Synaptic Device. *ACS Nano* **14**, 7628-7638, doi:10.1021/acsnano.0c03869 (2020).
  - 19 Fei, R., Kang, W. & Yang, L. Ferroelectricity and Phase Transitions in Monolayer Group-IV Monochalcogenides. *Physical Review Letters* **117**, 097601, doi:10.1103/PhysRevLett.117.097601 (2016).
  - 20 Bao, Y. *et al.* Gate-Tunable In-Plane Ferroelectricity in Few-Layer SnS. *Nano Letters* **19**, 5109-5117, doi:10.1021/acs.nanolett.9b01419 (2019).
  - 21 Chang, K. *et al.* Microscopic Manipulation of Ferroelectric Domains in SnSe Monolayers at Room Temperature. *Nano Letters* **20**, 6590-6597, doi:10.1021/acs.nanolett.0c02357 (2020).
  - 22 Chang, K. *et al.* Discovery of robust in-plane ferroelectricity in atomic-thick SnTe. *Science* **353**, 274-278, doi:doi:10.1126/science.aad8609 (2016).
  - 23 Yan, Y. *et al.* In-plane ferroelectricity in few-layered GeS and its van der Waals ferroelectric diodes. *Nanoscale* **13**, 16122-16130, doi:10.1039/D1NR03807A (2021).
  - 24 Guan, Z. *et al.* Electric-Field-Induced Room-Temperature Antiferroelectric–Ferroelectric Phase Transition in van der Waals Layered GeSe. *ACS Nano* **16**, 1308-1317, doi:10.1021/acsnano.1c09183 (2022).
  - 25 Gou, J. *et al.* Two-dimensional ferroelectricity in a single-element bismuth monolayer. *Nature* **617**, 67-72, doi:10.1038/s41586-023-05848-5 (2023).
  - 26 Sharma, P. *et al.* A room-temperature ferroelectric semimetal. *Science Advances* **5**, eaax5080, doi:doi:10.1126/sciadv.aax5080 (2019).
  - 27 Fei, Z. *et al.* Ferroelectric switching of a two-dimensional metal. *Nature* **560**, 336-339, doi:10.1038/s41586-018-0336-3 (2018).
  - 28 Niu, R. *et al.* Giant ferroelectric polarization in a bilayer graphene heterostructure. *Nature Communications* **13**, 6241, doi:10.1038/s41467-022-34104-z (2022).
  - 29 Zheng, Z. *et al.* Unconventional ferroelectricity in moiré heterostructures. *Nature* **588**, 71-76, doi:10.1038/s41586-020-2970-9 (2020).
  - 30 Yan, X. *et al.* Moiré synaptic transistor with room-temperature neuromorphic functionality. *Nature* **624**, 551-556, doi:10.1038/s41586-023-06791-1 (2023).
  - 31 Yang, T. H. *et al.* Ferroelectric transistors based on shear-transformation-mediated rhombohedral-stacked molybdenum disulfide. *Nature Electronics*, doi:10.1038/s41928-023-01073-0 (2023).

- 32 Deb, S. *et al.* Cumulative polarization in conductive interfacial ferroelectrics. *Nature* **612**, 465-469, doi:10.1038/s41586-022-05341-5 (2022).
- 33 Wang, X. *et al.* Interfacial ferroelectricity in rhombohedral-stacked bilayer transition metal dichalcogenides. *Nature Nanotechnology* **17**, 367-371, doi:10.1038/s41565-021-01059-z (2022).
- 34 McCreary, K. M. *et al.* Stacking-dependent optical properties in bilayer WSe<sub>2</sub>. *Nanoscale* **14**, 147-156, doi:10.1039/D1NR06119D (2022).